arXiv:astro-ph/0211159v1 8 Nov 2002

One-point Statistics of the Cosmic Density Field in Real and Redshift Spaces with A Multiresolutional Decomposition

Hu Zhan and Li-Zhi Fang

Department of Physics, University of Arizona, Tucson, AZ 85721

ABSTRACT

In this paper, we develop a method of performing the one-point statistics of a perturbed density field with a multiresolutional decomposition based on the discrete wavelet transform (DWT). We establish the algorithm of the one-point variable and its moments in considering the effects of Poisson sampling and selection function. We also establish the mapping between the DWT one-point statistics in redshift space and real space, i.e. the algorithm for recovering the DWT one-point statistics from the redshift distortion of bulk velocity, velocity dispersion, and selection function. Numerical tests on N-body simulation samples show that this algorithm works well on scales from a few hundreds to a few h^{-1} Mpc for four popular cold dark matter models.

Taking the advantage that the DWT one-point variable is dependent on both the scale and the shape (configuration) of decomposition modes, one can design estimators of the redshift distortion parameter (β) from combinations of DWT modes. Comparing with conventional β estimators, such as quadrupole-to-monopole ratio, the DWT β estimators are scale-decomposed. It is useful to consider scale-dependent effects. When the non-linear redshift distortion is not negligible, the quadrupole-to-monopole ratio is a function of scale. This estimator would not work without adding information about the scale-dependence, such as the power-spectrum index or the real-space correlation function of the random field. The DWT β estimators, however, do not need such extra information. Moreover, the scale-decomposed β estimators would also be able to reveal the scale-dependence of the bias parameter of galaxies. Numerical tests show that the proposed DWT estimators are able to determine β robustly with less than 15% uncertainty in the redshift range $0 \leq z \leq 3$.

Subject headings: cosmology: theory - large-scale structure of the universe

1. Introduction

The one-point probability distribution function (PDF) of a random mass density field $\rho(\mathbf{x})$, or the counts-in-cells (CiC) statistics of a discrete random distribution such as galaxies, is probably the first statistics used to reveal the clustering feature of galaxy distribution[1]. In the famous work by Edwin Hubble (1934), he showed that the frequency distribution of galaxy count N in angular cells is not Gaussian, but lognormal. This result indicates that the PDF of galaxy distribution is fundamental in characterizing the cosmic mass and velocity fields.

Although current samples applied for large-scale structure study have much deeper redshift and much wider angular size than available in Hubble's time, the one-point statistics is still frequently applied. This is because the one-point distribution and its moments contain complete information of the field, which might not be easily detected by other conventional methods. Unlike the Fourier amplitude, CiC is not subject to the central limit theorem. It can detect the non-Gaussianity of a field consisting of randomly distributed non-Gaussian clumps, while the PDF of the Fourier amplitudes is still Gaussian due to the central limit theorem (Fan and Bardeen 1995). Even the 2nd moment of one-point distribution is different from the 2nd moment of the Fourier decomposition – power spectrum. The former contains perturbations on scales larger than the size of the observed sample, while the latter does not. Therefore, one-point statistics is applied on various samples of large-scale structures, including galaxy surveys (e.g. Hamilton 1985; Alimi et al 1990; Gaztañaga 1992; Szapudi et al 1996; Kim & Strauss 1998), transmitted flux of quasars' Lyα absorption spectrum (e.g. Meiksin & Bouchet 1995; Gaztanñaga & Croft 1999; Zhan & Fang 2002), and N-body simulation samples (e.g. Coles & Jones 1991; Taylor & Watts 2000).

One-point statistics of a density fluctuation field $\delta(\mathbf{x})$ is given by the distribution of the one-point variable $\delta_R(\mathbf{x}_0)$, which is a sampling of the field by a window function $W_R(\mathbf{x}-\mathbf{x}_0)$ around position $\mathbf{x}_0$ and on scale R, i.e.

$$\delta_R(\mathbf{x}_0) = \int W_R(\mathbf{x}-\mathbf{x}_0)\delta(\mathbf{x})d\mathbf{x}. \tag{1}$$

The variable $\delta_R(\mathbf{x}_0)$ is actually a mean value of the field at position $\mathbf{x}_0$ and on scale R. The distribution of $\delta_R(\mathbf{x}_0)$ gives a PDF description of the field.

Eq.(1) is a space($\mathbf{x}_0$)-scale(R) decomposition of the field $\delta(\mathbf{x})$ with bases $W_R(\mathbf{x}_0)$. Most popular windows $W_R(\mathbf{x}-\mathbf{x}_0)$ are Gaussian and top-hat filters. The Gaussian windows gener-

[1]Since we study only the one-point PDF in this paper, not N-point PDF, hereafter, PDF stands only for the one-point statistics.

ally are not orthogonal, i.e. the function $W_R(\mathbf{x}-\mathbf{x}_0)$ does not satisfy $\int W_R(\mathbf{x}-\mathbf{x}_1)W_R(\mathbf{x}-\mathbf{x}_2)d\mathbf{x} = 0$, if $\mathbf{x_1} \neq \mathbf{x_2}$. Thus, the variables $\delta_R(\mathbf{x}_0)$ are either incomplete or redundant. In turn, these may lead to 1) loss of information of the field $\delta(\mathbf{x})$; and 2) false correlation. It is possible to construct an orthogonal and complete set of bases from top-hat windows. However, they are not localized in the Fourier space. The index R does not refer to a well defined scale k. As a consequence, the one-point statistics with conventional windows are not suitable for problems with a scale-dependence. For instance, the redshift distortion on the one-point statistics can be properly estimated only if we know how the redshift distortion depends on the scale and shape of the window function. Therefore, a better algorithm for the one-point statistics is needed, for example, to recover the real-space rms density fluctuation σ_8 from redshift distortion.

In this paper, we show that these problems can be solved with a multiresolutional decomposition via the discrete wavelet transform (DWT). The bases of the DWT decomposition are complete, orthogonal, and localized in both physical and Fourier spaces. It was shown in the last few years that the DWT can be employed as an alternative representation in most conventional statistics of cosmic mass and velocity fields, including power spectrum (Pando & Fang 1998; Fang & Feng 2000; Yang et al 2001a, 2002), high order correlations (Pando & Fang 1998; Pando, Feng & Fang 2001; Feng, Pando & Fang 2001), bulk and pair-wise velocity (Zhan & Fang 2002; Yang et al. 2001b), and identification of halos and clusters (Xu, Fang & Wu 2000). The DWT representation is also able to reveal statistical features, which might not be easily detected without a set of decomposition bases localized in both physical and scale spaces. With the DWT analysis, the intermittency of the fluctuations of quasars' Lyα transmitted flux has been detected (Jamkhedkar, Zhan & Fang 2000; Pando, Feng & Fang 2000; Zhan, Jamkhedkar & Fang 2001; Pando et al. 2002). This property cannot be simply detected by the popular $W_R(\mathbf{x}-\mathbf{x}_0)$ or Fourier decompositions.

We also show that the DWT decomposition is very useful for one-point statistics. We establish the algorithm of the one-point variable and its moments in considering various corrections, such as Poisson sampling and selection function. To demonstrate the advantage of the DWT one-point statistics, we show that one can map between the one-point statistics in real and redshift spaces scale-by-scale, taking account the distortion due to bulk velocity, velocity dispersion and selection function. With these results one can construct β (redshift distortion parameter) estimators with moments of the DWT one-point variables. Unlike conventional estimators, the DWT estimators do not need extra-information or *ad hoc* assumption when the non-linear redshift distortion is not negligible.

This paper is organized as follows. §2 presents the algorithm for the PDF of one-point variables with the DWT space-scale decomposition. §3 discusses the second moment of the

one-point variables in considering the effects of Poisson sampling and selection function. In §4 we develop the theory of redshift distortion of the DWT one-point variables. §5 tests the theoretical results in §4 on N-body simulation samples. The emphases are the redshift-to-real-space mapping of the diagonal and off-diagonal second moments. §6 shows the application in estimating the redshift distortion parameter. Finally, the conclusions and discussions are given in §7. The Appendix provides relevant formulae for quantities defined in §4. We release the codes for calculating these quantities via anonymous ftp at samuri.la.asu.edu/pub/zhan/DWTCiC.tgz.

2. One-point statistics in the DWT representation

2.1. DWT variable of one-point statistics

As emphasized in §1, a key problem for one-point statistics is to have proper window functions $W_R(\mathbf{x})$, and define the variable with eq.(1). In the DWT analysis, this is done by the so-called scaling function. Let us first briefly introduce the DWT-decomposition of a random field. For the details of the mathematical properties of the DWT see Mallat (1989a,b); Meyer (1992); Daubechies (1992), and for physical applications see Fang & Thews (1998).

To simplify the notation, we first consider a one-dimensional (1-D) density fluctuation $\delta(x)$ on a spatial range from $x = 0$ to L. We first divide the space L into 2^j segments labeled by $l = 0, 1, ...2^j - 1$. Each segment is of size $L/2^j$. The index j can be a positive integer. It stands for a length scale $L/2^j$. The higher the j, the smaller the length scale. Even though we often refer some properties to a (range of) j in the analyses below, it must be read as an association of the properties with the length scale $L/2^j$. The index l is for position, and it corresponds to the spatial range $lL/2^j < x < (l+1)L/2^j$. That is, the space L is decomposed into cells (j, l).

In the DWT analysis, each cell (j, l) supports two compact functions: the scaling function $\phi_{j,l}(x)$ and the wavelet $\psi_{j,l}(x)$. One example of such functions is the Daubechies 4 (D4) wavelets[2], which have to be constructed recursively (Daubechies 1992; see also Fang & Thews 1998). The properties of D4 wavelets are listed below and in the appendix §A.1. We show, in Fig. 1, examples of the D4 scaling function and wavelet, and their Fourier transform $\hat{\phi}_{j,l}(k)$ and $\hat{\psi}_{j,l}(k)$. One can see from Fig. 1 that both the scaling function and the wavelet

[2]Unless mentioned in contrast to the scaling functions, wavelets, as analysis tools, always involve the scaling functions.

are localized in Fourier space as well as in physical space. Generally, $\phi_{j,l}(x)$ and $\psi_{j,l}(x)$ are localized in cell (j,l), $\hat{\phi}_{j,l}(k)$ is localized in the scale range $|k| \leq 2\pi 2^j/L$, and $\hat{\psi}_{j,l}(k)$ in the range $k \pm k/2$, where $|k| = 2\pi 2^j/L$.

Obviously, the scaling function $\phi_{j,l}(x)$ is a window function on scale j and around the segment l. It can be used to measure the mean field in cell (j,l)

$$\delta_{j,l} = \frac{\int_0^L \delta(x)\phi_{j,l}(x)dx}{\int_0^L \phi_{j,l}(x)dx} = \frac{1}{\int_0^L \phi_{j,l}(x)dx}\epsilon_{j,l}, \tag{2}$$

where $\epsilon_{j,l}$ is called scaling function coefficient (SFC), given by

$$\epsilon_{j,l} = \int_0^L \delta(x)\phi_{j,l}(x)dx. \tag{3}$$

In analogous to eq.(1), eqs.(2) and (3) show that the SFC $\epsilon_{j,l}$ or δ_{jl} can be employed as the variable for one-point statistics.

Fig. 1 also demonstrates that wavelets are admissible, i.e. $\int \psi_{j,l}(x)dx = 0$, and therefore, they are used to measure the fluctuations of a field with respect to its mean in cells (j,l)

$$\tilde{\epsilon}_{j,l} = \int \delta(x)\psi_{j,l}(x)dx, \tag{4}$$

where $\tilde{\epsilon}_{j,l}$ is called the wavelet function coefficient (WFC).

The scaling function $\phi_{j,l}(x)$ and the wavelet $\psi_{j,l}(x)$ satisfy a set of orthonormal relations as

$$\int \phi_{j,l}(x)\phi_{j,l'}(x)dx = \delta^K_{l,l'}, \tag{5}$$

$$\int \psi_{j,l}(x)\psi_{j',l'}(x)dx = \delta^K_{j,j'}\delta^K_{l,l'}, \tag{6}$$

$$\int \phi_{j,l}(x)\psi_{j',l'}(x)dx = 0, \qquad \text{if } j' \geq j, \tag{7}$$

where $\delta^K_{m,n}$ is the Kronecker delta function. To be consistent with eq.(5), the scaling function $\phi_{j,l}(x)$ is normalized to

$$\int \phi_{j,l}(x)dx = \sqrt{\frac{L}{2^j}}. \tag{8}$$

With these properties, a 1-D density field $\delta(x)$ can be decomposed into

$$\delta(x) = \sum_{l=0}^{2^j-1} \epsilon_{j,l}\phi_{j,l}(x) + \sum_{j'=j}^{\infty}\sum_{l=0}^{2^{j'}-1} \tilde{\epsilon}_{j',l}\psi_{j',l}(x). \tag{9}$$

The second term on the r.h.s of eq.(9) contains only the information of the field $\delta(x)$ on scales equal to and less than $L/2^j$. Therefore, the 2^j variables (SFCs) $\epsilon_{j,l}$, with $l = 0...2^j - 1$, completely describe the behavior of the field on scales larger than $L/2^j$. For instance, if the resolution of the sample is $L/2^J$, $\delta(x)$ can be described by the 2^J SFCs $\epsilon_{J,l}$. Because of the orthogonal relation eqs.(5) and (7), the 2^j variables (SFCs) $\epsilon_{j,l}$ are independent and irredundant.

In a functional space consisting of functions, which are smoothed on scales equal to and less than $L/2^j$, the completeness of the scaling function $\phi_{j,l}(x)$ can be expressed as

$$\sum_{l=0}^{2^j-1} \phi_{j,l}(x)\phi_{j,l}(x') = \delta^D(x - x'), \tag{10}$$

where $\delta^D(x - x')$ is the Dirac Delta function.

All the above-mentioned results can be easily generalized to three-dimensional (3-D) fields. Let us consider a 3-D distribution $\delta(\mathbf{x})$ in a volume $\mathbf{x} = (0, 0, 0)$ to (L_1, L_2, L_3). Similar to the 1-D case, we divide the volume $L_1 \times L_2 \times L_3$ into cells $(\mathbf{j}, \mathbf{l})$, where $\mathbf{j} = (j_1, j_2, j_3)$ refers to the length scale $(L_1/2^{j_1}, L_2/2^{j_2}, L_3/2^{j_3})$, and $\mathbf{l} = (l_1, l_2, l_3)$ refers to the spatial range of the cell, $l_i L_i/2^{j_i} < x_i \leq (l_i + 1)L_i/2^{j_i}$ and $l_i = 0...2^{j_i} - 1$, where $i = 1, 2, 3$. The one-point statistical variable of the field $\delta(\mathbf{x})$ is

$$\epsilon_{\mathbf{j},\mathbf{l}} = \int \delta(\mathbf{x})\phi_{\mathbf{j},\mathbf{l}}(\mathbf{x})d\mathbf{x}, \tag{11}$$

where the 3-D scaling function (3-D window) $\phi_{\mathbf{j},\mathbf{l}}(\mathbf{x})$ is given by a direct product of 1-D scaling functions as

$$\phi_{\mathbf{j},\mathbf{l}}(\mathbf{x}) = \phi_{j_1,l_1}(x_1)\phi_{j_2,l_2}(x_2)\phi_{j_3,l_3}(x_3). \tag{12}$$

One can also construct 3-D wavelets $\psi_{\mathbf{j},\mathbf{l}}(\mathbf{x})$ as a direct product of 1-D scaling functions and wavelets (see Yang et al 2002), and generalize eq.(9) into 3-D as

$$\delta(\mathbf{x}) = \sum_{l_1=0}^{2^{j_1}-1} \sum_{l_2=0}^{2^{j_2}-1} \sum_{l_3=0}^{2^{j_3}-1} \epsilon_{\mathbf{j},\mathbf{l}}\phi_{\mathbf{j},\mathbf{l}}(\mathbf{x}) + \text{terms of } \psi_{\mathbf{j}',\mathbf{l}'} \text{ with } j_i' \geq j_i. \tag{13}$$

Since the second term on the r.h.s. is not needed in calculating the one-point statistics, therefore, we do not show the details of $\psi_{\mathbf{j}',\mathbf{l}'}$, but only give the orthogonal relations

$$\int \phi_{\mathbf{j},\mathbf{l}}(\mathbf{x})\psi_{\mathbf{j}',\mathbf{l}'}(\mathbf{x})d\mathbf{x} = 0, \quad \text{if } j_i' \geq j_i,\ i = 1, 2, 3. \tag{14}$$

If we consider only functions smoothed on scales equal to and less than the scale of $\mathbf{j}$ in each dimension, the set of bases $\phi_{\mathbf{j},\mathbf{l}}(\mathbf{x})$ is orthogonal and complete.

2.2. Moments of DWT one-point distribution

In one-point statistics, the statistical feature of the field $\delta(\mathbf{x})$ is characterized by the moments of the distribution of $\epsilon_{\mathbf{j},\mathbf{l}}$. The mth moment is $\langle\epsilon^m_{\mathbf{j},\mathbf{l}}\rangle$, where $\langle ...\rangle$ stands for an ensemble average. Using eq.(11), we have

$$\langle\epsilon^m_{\mathbf{j},\mathbf{l}}\rangle = \int \langle\delta(\mathbf{x}_1)...\delta(\mathbf{x}_m)\rangle\phi_{\mathbf{j},\mathbf{l}}(\mathbf{x}_1)...\phi_{\mathbf{j},\mathbf{l}}(\mathbf{x}_m)d\mathbf{x}_1...d\mathbf{x}_m. \tag{15}$$

For a homogeneous field, these moments are $\mathbf{l}$-independent. Moreover, when the "fair sample hypothesis" (Peebles 1980) holds, or equivalently, when the random field is ergodic, the $2^{j_1+j_2+j_3}$ SFCs $\epsilon_{\mathbf{j},\mathbf{l}}$, $l_i = 0...2^{j_i}-1$, $i = 1, 2, 3$ for a given scale $\mathbf{j}$ can be considered as $2^{j_1+j_2+j_3}$ independent measurements, because they are measured by projecting onto the mutually orthogonal basis $\phi_{\mathbf{j},\mathbf{l}}(\mathbf{x})$. Accordingly, the $2^{j_1+j_2+j_3}$ SFCs form a statistical ensemble on the scale $\mathbf{j}$. This ensemble represents actually the one-point distribution of $\epsilon_{\mathbf{j},\mathbf{l}}$ over the DWT modes at a given scale $\mathbf{j}$. Thus, the average over $\mathbf{l}$ is a fair estimation of the ensemble average, i.e.

$$\langle\epsilon^m_{\mathbf{j},\mathbf{l}}\rangle = \frac{1}{2^{j_1+j_2+j_3}}\sum_{l_1=0}^{2^{j_1}-1}\sum_{l_2=0}^{2^{j_2}-1}\sum_{l_3=0}^{2^{j_3}-1}\epsilon^m_{\mathbf{j},\mathbf{l}}. \tag{16}$$

We now consider the 2nd moment $\langle\epsilon^2_{\mathbf{j},\mathbf{l}}\rangle$. From eq.(15), the 2nd moment is determined by the usual two point correlation function $\langle\delta(\mathbf{x}_1)\delta(\mathbf{x}_2)\rangle$. We define a dimensionless 2nd moment on scale $\mathbf{j}$ by

$$D_{\mathbf{j}} \equiv \frac{2^{(j_1+j_2+j_3)}}{L_1L_2L_3}\langle\epsilon^2_{\mathbf{j},\mathbf{l}}\rangle = \frac{1}{L_1L_2L_3}\sum_{l_1=0}^{2^{j_1}-1}\sum_{l_2=0}^{2^{j_2}-1}\sum_{l_3=0}^{2^{j_3}-1}\epsilon^2_{\mathbf{j},\mathbf{l}}. \tag{17}$$

Using eqs.(12) and (15), one can rewrite eq.(17) as

$$D_{\mathbf{j}} = \frac{1}{L_1L_2L_3}\sum_{n_1=-\infty}^{\infty}\sum_{n_2=-\infty}^{\infty}\sum_{n_3=-\infty}^{\infty}|\hat{\phi}(n_1/2^{j_1})\hat{\phi}(n_2/2^{j_2})\hat{\phi}(n_3/2^{j_3})|^2P(n_1,n_2,n_3), \tag{18}$$

where $\hat{\phi}(n)$ is the Fourier transform of the basic scaling function (see eq.(A1) in Appendix A). The term $P(n_1, n_2, n_3)$ in eq. (18) is the Fourier power spectrum defined by

$$P(n_1,n_2,n_3) = \langle\hat{\delta}(\mathbf{k})\hat{\delta}^\dagger(\mathbf{k})\rangle, \tag{19}$$

where $\mathbf{k} = (k_1, k_2, k_3)$ with $k_i = 2\pi n_i/L_i$, and

$$\hat{\delta}(\mathbf{k}) = \frac{1}{L_1L_2L_3}\int_0^{L_1}\int_0^{L_2}\int_0^{L_3}\delta(\mathbf{x})e^{-i\mathbf{k}\cdot\mathbf{x}}d\mathbf{x}. \tag{20}$$

One can compare the 2nd moment $D_{\mathbf{j}}$ with the DWT power spectrum given by Fang & Feng (2000) as

$$P_{\mathbf{j}} = \frac{1}{2^{j_1+j_2+j_3}} \sum_{n_1=-\infty}^{\infty} \sum_{n_2=-\infty}^{\infty} \sum_{n_3=-\infty}^{\infty} |\hat{\psi}(n_1/2^{j_1})\hat{\psi}(n_2/2^{j_2})\hat{\psi}(n_3/2^{j_3})|^2 P(n_1, n_2, n_3), \qquad (21)$$

where $\hat{\psi}(n)$ is the Fourier transform of the basic wavelet. Therefore, both the DWT power spectrum and the DWT one-point statistics can be calculated with a single DWT decomposition. The former relies on the wavelet, while the latter on the scaling function.

The Fourier transform of the scaling function $\hat{\phi}(n)$ is non-zero in n-space where $|n| \leq 1$, and $\hat{\psi}(n)$ is mainly in $1/2 < |n| < 1$ (Fig. 1 and eq.(A4)). Therefore, the DWT power spectrum P_j is actually a banded Fourier power spectrum in the wavenumber range $\pi 2^{j_i}/L_i < |k_i| < \pi 2^{j_i+1}/L_i$, while the 2nd moment D_j contains all powers with $|k_i| \leq \pi 2^{j_i+1}/L_i$. It is well known that the 2nd moment of one-point statistics, such as $D_{\mathbf{j}}$ or σ_8, is sensitive to long wavelength behavior of the perturbations. This can also be seen from the relation between the scaling functions and wavelets as follows

$$|\hat{\phi}_{j,0}(k)|^2 = \frac{1}{2}|\hat{\psi}_{j-1,0}(k)|^2 + \frac{1}{2}|\hat{\phi}_{j-1,0}(k)|^2 = \sum_{n=1}^{j} \frac{1}{2^n}|\hat{\psi}_{j-n,0}(k)|^2 + \frac{1}{2^j}|\hat{\phi}_{0,0}(k)|^2. \qquad (22)$$

That is, the factor $|\hat{\phi}_{j,0}(k)|^2$ in eq.(22) extracts all powers on scales larger than $L/2^j$. Eq.(22) holds only for compactly supported discrete wavelets such as Daubechies wavelets.

3. One-point statistics of galaxy distribution in the DWT representation

3.1. Galaxy distribution

We now consider distributions of discrete objects, such as simulation particles and observed or mock galaxies. If the position measurement of particles or galaxies is perfectly precise, the number density distribution of these samples can be written as

$$n^g(\mathbf{x}) = \sum_{m=1}^{N_g} w_m \delta^D(\mathbf{x} - \mathbf{x}_m) = \bar{n}(\mathbf{x})[1 + \delta(\mathbf{x})], \qquad (23)$$

where N_g is the total number of the particles or galaxies, $\mathbf{x}_m$ is the position of the mth galaxy, w_m is its weight, and $\bar{n}(\mathbf{x})$ is the selection function, which is given by the mean number density of galaxies when galaxy clustering is absent, and $\delta(\mathbf{x})$ is the density fluctuation in the distribution.

One can subject $n^g(\mathbf{x})$ to a DWT decomposition. Similar to eq.(13), we have

$$n^g(\mathbf{x}) = \sum_{l_1=0}^{2^{j_1}-1} \sum_{l_2=0}^{2^{j_2}-1} \sum_{l_3=0}^{2^{j_3}-1} \epsilon^g_{\mathbf{j},\mathbf{l}} \phi_{\mathbf{j},\mathbf{l}}(\mathbf{x}) + \text{terms of } \psi_{\mathbf{j}',\mathbf{l}'} \text{ with } j'_i \geq j_i, \tag{24}$$

where

$$\epsilon^g_{\mathbf{j},\mathbf{l}} = \int n^g(\mathbf{x}) \phi_{\mathbf{j},\mathbf{l}}(\mathbf{x}) d\mathbf{x} = \sum_{m=1}^{N_g} w_m \phi_{\mathbf{j},\mathbf{l}}(\mathbf{x}_m). \tag{25}$$

The DWT one-point variables of $\delta(\mathbf{x})$ is now given by

$$\epsilon_{\mathbf{j},\mathbf{l}} = \int \delta(\mathbf{x}) \phi_{\mathbf{j},\mathbf{l}}(\mathbf{x}) d\mathbf{x} = \int \left[\frac{n^g(\mathbf{x})}{\bar{n}(\mathbf{x})} - 1 \right] \phi_{\mathbf{j},\mathbf{l}}(\mathbf{x}) d\mathbf{x}. \tag{26}$$

Since the selection function varies slowly, we have

$$\int \frac{n^g(\mathbf{x})}{\bar{n}(\mathbf{x})} \phi_{\mathbf{j},\mathbf{l}}(\mathbf{x}) d\mathbf{x} \simeq \frac{1}{\bar{n}_{\mathbf{j},\mathbf{l}}} \int n^g(\mathbf{x}) \phi_{\mathbf{j},\mathbf{l}}(\mathbf{x}) d\mathbf{x} = \frac{\epsilon^g_{\mathbf{j},\mathbf{l}}}{\bar{n}_{\mathbf{j},\mathbf{l}}}, \tag{27}$$

where $\bar{n}_{\mathbf{j},\mathbf{l}}$ is the mean of the selection faction in the cell $(\mathbf{j},\mathbf{l})$. The algorithm for $\bar{n}_{\mathbf{j},\mathbf{l}}$ is given in next subsection. Substituting eq.(27) into eq.(26) we have

$$\epsilon_{\mathbf{j},\mathbf{l}} \simeq \frac{\epsilon^g_{\mathbf{j},\mathbf{l}}}{\bar{n}_{\mathbf{j},\mathbf{l}}} - \sqrt{\frac{L_1 L_2 L_3}{2^{j_1+j_2+j_3}}}. \tag{28}$$

The second term on the r.h.s. is due the normalization of the scaling function eq.(8).

3.2. Selection function in the DWT representation

By definition of equation (23), selection function $\bar{n}(\mathbf{x})$ is the galaxy distribution if galaxy clustering $\delta(\mathbf{x})$ is absent. In the plane-parallel approximation, selection function depends only on x_3, i.e. the coordinate in the redshift direction or the line-of-sight (LOS). Thus, from equation (23) the selection function $\bar{n}(x_3)$ can be approximated by an average of $n^g(\mathbf{x})$ over the plane (x_1, x_2), which depends upon the geometry of a real survey. In a simple case, for example, a mock survey in a simulation box, it reads

$$\bar{n}(x_3) = \frac{1}{L_1 L_2} \int_0^{L_1} \int_0^{L_2} n^g(\mathbf{x}) dx_1 dx_2. \tag{29}$$

With eq.(24), eq.(29) yields

$$\bar{n}(x_3) = \sum_{l_3=0}^{2^{j_3}-1} \epsilon^g_{00 j_3, 00 l_3} \phi_{j_3,l_3}(x_3). \tag{30}$$

By definition, $\bar{n}_{\mathbf{j},\mathbf{l}}$ is the mean of $\bar{n}(x_3)$ in the cell $(\mathbf{j},\mathbf{l})$. Using eq. (30), we have

$$\bar{n}_{\mathbf{j},\mathbf{l}} = \sqrt{\frac{2^{j_1+j_2+j_3}}{L_1L_2L_3}} \int \bar{n}(x_3)\phi_{j,l}(\mathbf{x})d\mathbf{x} = \sqrt{\frac{2^{j_3}}{L_3}}\epsilon^g_{00j_3,00l_3}. \tag{31}$$

That is, the selection function can be approximately expressed by the SFC of the (observable) galaxy distribution $n^g(\mathbf{x})$.

3.3. Effect of Poisson sampling

The observed galaxy distributions $n^g(\mathbf{x})$ are considered to be a Poisson sampling with an intensity $n(\mathbf{x}) = \bar{n}(\mathbf{x})[1+\delta(\mathbf{x})]$. In this case, the characteristic function of the galaxy distribution $n^g(\mathbf{x})$ is

$$\langle [e^{i\int n^g(\mathbf{x})u(\mathbf{x})d\mathbf{x}}]\rangle_P = \exp\left\{\int d\mathbf{x} n(\mathbf{x})[e^{iu(\mathbf{x})}-1]\right\}, \tag{32}$$

where $\langle ...\rangle_P$ is the average for the Poisson sampling. The m-point correlation functions of $n^g(\mathbf{x})$ are given by

$$\langle n^g(\mathbf{x}_1)...n^g(\mathbf{x}_m)\rangle_P = \frac{1}{i^m}\left[\frac{\delta^m Z}{\delta u(\mathbf{x}_1)...\delta u(\mathbf{x}_m)}\right]_{u=0}. \tag{33}$$

We have then

$$\langle n^g(\mathbf{x})\rangle_P = n(\mathbf{x}), \tag{34}$$

and

$$\langle n^g(\mathbf{x})n^g(\mathbf{x}')\rangle_P = n(\mathbf{x})n(\mathbf{x}') + \delta^D(\mathbf{x}-\mathbf{x}')n(\mathbf{x}). \tag{35}$$

Substituting $n(\mathbf{x}) = \bar{n}(\mathbf{x})[1+\delta(\mathbf{x})]$ into eq.(35), we have

$$\langle \delta(\mathbf{x})\delta(\mathbf{x}')\rangle = \left\langle \frac{\langle n^g(\mathbf{x})n^g(\mathbf{x}')\rangle_P}{\bar{n}(\mathbf{x})\bar{n}(\mathbf{x}')}\right\rangle - \left\langle \delta^D(\mathbf{x}-\mathbf{x}')\frac{1}{\bar{n}(\mathbf{x})}\right\rangle - 1. \tag{36}$$

Subjecting eq.(36) to a scaling function projection, and using eq.(27), we have approximately

$$\langle \epsilon_{\mathbf{j},\mathbf{l}}\epsilon_{\mathbf{j}',\mathbf{l}'}\rangle = \left\langle \left\langle \frac{\epsilon^g_{\mathbf{j},\mathbf{l}}}{\bar{n}_{\mathbf{j},\mathbf{l}}}\frac{\epsilon^g_{\mathbf{j}',\mathbf{l}'}}{\bar{n}_{\mathbf{j}',\mathbf{l}'}}\right\rangle_P\right\rangle - \left\langle \frac{1}{\bar{n}_{\mathbf{j},\mathbf{l}}}\right\rangle - \frac{L_1L_2L_3}{2^{j_1+j_2+j_3}}. \tag{37}$$

The last term in eq.(37) is due to the normalization eq.(8). From eq.(37), the 2nd moment $D_{\mathbf{j}}$ is given by

$$D_{\mathbf{j}} = \frac{1}{L_1L_2L_3}\sum_{l_1=0}^{2^{j_1}-1}\sum_{l_2=0}^{2^{j_2}-1}\sum_{l_3=0}^{2^{j_3}-1}\left[\left(\frac{\epsilon^g_{\mathbf{j},\mathbf{l}}}{\bar{n}_{\mathbf{j},\mathbf{l}}}\right)^2 - \frac{1}{\bar{n}_{\mathbf{j},\mathbf{l}}}\right] - 1. \tag{38}$$

The second term on the r.h.s. under the summation is the correction due to Poisson noise, and the rest is the normalized 2nd moment of $\delta(\mathbf{x})$. One can also calculate the Poisson correction for higher order moments with eq.(33).

4. Redshift distortion of one-point statistics

4.1. DWT CiC variables in redshift space

Actually, astronomical data often gives only the distribution in redshift space, i.e.

$$n^S(\mathbf{s}) = \sum_{m=1}^{N_g} w_m \delta_D[\mathbf{s} - \mathbf{x}_m - \hat{\mathbf{r}} v_r(\mathbf{x}_m)/H] = \bar{n}^S(\mathbf{s})[1 + \delta^S(\mathbf{s})], \tag{39}$$

where $v_r(\mathbf{x}_i)$ is the radial ($\hat{\mathbf{r}}$) component of the velocity of the ith galaxy, $\bar{n}^S(\mathbf{s})$ is the selection function in redshift space, and H is the Hubble constant at the corresponding redshift. Thus, we can only calculate the CiC moments in redshift space.

For a given mass field $\delta(\mathbf{x})$, the galaxy velocity $\mathbf{v}(\mathbf{x})$ is a random field with mean

$$\mathbf{V}(\mathbf{x}) = \langle \mathbf{v}(\mathbf{x}) \rangle_v, \tag{40}$$

where $\langle .. \rangle_v$ is the average over the ensemble of velocities. The mean velocity $\mathbf{V}(\mathbf{x})$ is also called bulk velocity at $\mathbf{x}$, which is assumed irrotational (Bertschinger & Dekel 1989; Dekel, Bertschinger & Faber 1990; Dekel et al. 1999). In linear regime, the bulk velocity is related to the density contrast by

$$\delta(\mathbf{x}) = -\frac{1}{H\beta} \nabla \cdot \mathbf{V}(\mathbf{x}), \tag{41}$$

where the parameter $\beta \simeq \Omega^{0.6}/b$ at present, i.e. redshift $z = 0$, and b is the linear bias parameter. The *rms* deviation of velocity $\mathbf{v}(\mathbf{x})$ from the bulk velocity $\mathbf{V}(\mathbf{x})$ is

$$\langle [v_i(\mathbf{x}) - V_i(\mathbf{x})]^2 \rangle_v = [\sigma^{v_i}(\mathbf{x})]^2, \ i = 1, 2, 3. \tag{42}$$

In order to express the scale dependence of the bulk velocity $V_i(\mathbf{x})$ and the variance $\sigma^v(\mathbf{x})$, we can also decompose the velocity field $\mathbf{v}(\mathbf{x})$ with a DWT, i.e.

$$\epsilon^{v_i}_{\mathbf{j},\mathbf{l}} = \int v_i(\mathbf{x}) \phi_{\mathbf{j},\mathbf{l}}(\mathbf{x}) d\mathbf{x}. \tag{43}$$

Obviously, the variance $\sigma^v(\mathbf{x})$ on scale $\mathbf{j}$ is given by

$$\sigma^v_{\mathbf{j}} = \left[\sum_{i=1}^{3} \langle v_i^2 \rangle_v - \frac{2^{j_1+j_2+j_3}}{L_1 L_2 L_3} \sum_{i=1}^{3} \langle \epsilon^{v_i}_{\mathbf{j},\mathbf{l}} \rangle_v^2 \right]^{1/2}. \tag{44}$$

Although $\epsilon^{v_i}_{\mathbf{j},\mathbf{l}}$ is $\mathbf{l}$-dependent, $\sigma^v_{\mathbf{j}}$ should be $\mathbf{l}$-independent if the random field $\mathbf{v}(\mathbf{x})$ is ergodic. On large scales, say $\geq 10 \mathrm{h}^{-1}$Mpc, the velocity field $\mathbf{v}(\mathbf{x})$ is roughly *Gaussian*, and it can be described by its mean and variance, which are generally scale-dependent.

4.2. Redshift distortion without selection function effect

Because of eq.(39), the directly measurable DWT variable is not given by eqs. (26) or (28), but

$$\epsilon^S_{\mathbf{j},\mathbf{l}} = \int \delta^S(\mathbf{s})\phi_{\mathbf{j},\mathbf{l}}(\mathbf{s})d\mathbf{s} = \int \left[n^S(\mathbf{s})/\bar{n}^S(\mathbf{s}) - 1\right]\phi_{\mathbf{j},\mathbf{l}}(\mathbf{s})d\mathbf{s} \tag{45}$$
$$= \frac{1}{\bar{n}^S_{\mathbf{j},\mathbf{l}}}\sum_{m=1}^{N_g} w_m \phi_{\mathbf{j},\mathbf{l}}(\mathbf{x}_m + \hat{\mathbf{r}}v_r(\mathbf{x}_m)/H) - \sqrt{\frac{L_1L_2L_3}{2^{j_1+j_2+j_3}}}.$$

where $\bar{n}^S_{\mathbf{j},\mathbf{l}}$ is calculated in the same way as eq.(31), but with $n^S(\mathbf{s})$ to replace $n^g(\mathbf{x})$.

In this section, we do not consider the effect of selection function, i.e. $\bar{n} = const.$ In the plane-parallel approximation, i.e. $\hat{\mathbf{r}}$ is along the $\hat{x_3}$-direction, eq.(45) becomes

$$\epsilon^S_{\mathbf{j},\mathbf{l}} = \frac{1}{\bar{n}}\int n^g(\mathbf{x}) e^{v_3(\mathbf{x})\frac{1}{H}\frac{\partial}{\partial x_3}}\phi_{\mathbf{j},\mathbf{l}}(\mathbf{x})d\mathbf{x} - \sqrt{\frac{L_1L_2L_3}{2^{j_1+j_2+j_3}}}. \tag{46}$$

If the velocity field is Gaussian, subjecting eq.(46) to an average over the ensemble of velocities, we have

$$\langle\epsilon^S_{\mathbf{j},\mathbf{l}}\rangle_v = \frac{1}{\bar{n}}\int n^g(\mathbf{x})\langle e^{v_3(\mathbf{x})\frac{1}{H}\frac{\partial}{\partial x_3}}\rangle_v \phi_{\mathbf{j},\mathbf{l}}(\mathbf{x})d\mathbf{x} - \sqrt{\frac{L_1L_2L_3}{2^{j_1+j_2+j_3}}} \tag{47}$$
$$= \int [1+\delta(\mathbf{x})] e^{V_3(\mathbf{x})\frac{1}{H}\frac{\partial}{\partial x_3} + \frac{1}{2}(\sigma^{v_3}_{\mathbf{j}}/H)^2\left(\frac{\partial}{\partial x_3}\right)^2}\phi_{\mathbf{j},\mathbf{l}}(\mathbf{x})d\mathbf{x} - \sqrt{\frac{L_1L_2L_3}{2^{j_1+j_2+j_3}}}.$$

For clarity, the angle brackets $\langle\ldots\rangle_v$ are dropped hereafter without causing any confusion.

If we consider only the linear effect of the bulk velocity, equation (47) is approximately

$$\epsilon^S_{\mathbf{j},\mathbf{l}} \simeq \int [1+\delta(\mathbf{x})]\left[1 + V_3(\mathbf{x})\frac{1}{H}\frac{\partial}{\partial x_3}\right] e^{\frac{1}{2}(\sigma^{v_3}_{\mathbf{j}}/H)^2\left(\frac{\partial}{\partial x_3}\right)^2}\phi_{\mathbf{j},\mathbf{l}}(\mathbf{x})d\mathbf{x} - \sqrt{\frac{L_1L_2L_3}{2^{j_1+j_2+j_3}}}. \tag{48}$$

Neglecting the terms of the order of $V_3(\mathbf{x})\delta(\mathbf{x})$, and using the linear relation between $\delta(\mathbf{x})$ and $\mathbf{V}(\mathbf{x})$, we have

$$\epsilon^S_{\mathbf{j},\mathbf{l}} \simeq \int \left\{1 + \delta(\mathbf{x}) - \beta\left[\nabla^{-2}\frac{\partial}{\partial x_3}\delta(\mathbf{x})\right]\frac{\partial}{\partial x_3}\right\} e^{\frac{1}{2}(\sigma^{v_3}_{\mathbf{j}}/H)^2\left(\frac{\partial}{\partial x_3}\right)^2}\phi_{\mathbf{j},\mathbf{l}}(\mathbf{x})d\mathbf{x} - \sqrt{\frac{L_1L_2L_3}{2^{j_1+j_2+j_3}}} \tag{49}$$
$$= \int e^{\frac{1}{2}(\sigma^{v_3}_{\mathbf{j}}/H)^2\left(\frac{\partial}{\partial x_3}\right)^2}\phi_{\mathbf{j},\mathbf{l}}(\mathbf{x})d\mathbf{x} + \sum_{\mathbf{l}'}\epsilon_{\mathbf{j},\mathbf{l}'}\int \phi_{\mathbf{j},\mathbf{l}'}(\mathbf{x}) e^{\frac{1}{2}(\sigma^{v_3}_{\mathbf{j}}/H)^2\left(\frac{\partial}{\partial x_3}\right)^2}\phi_{\mathbf{j},\mathbf{l}}(\mathbf{x})d\mathbf{x}$$
$$+\beta\sum_{\mathbf{l}'}\epsilon_{\mathbf{j},\mathbf{l}'}\int \phi_{\mathbf{j},\mathbf{l}'}(\mathbf{x}) e^{\frac{1}{2}(\sigma^{v_3}_{\mathbf{j}}/H)^2\left(\frac{\partial}{\partial x_3}\right)^2}\nabla^{-2}\frac{\partial^2}{\partial x_3^2}\phi_{\mathbf{j},\mathbf{l}}(\mathbf{x})d\mathbf{x} - \sqrt{\frac{L_1L_2L_3}{2^{j_1+j_2+j_3}}}.$$

In the last step, integration by parts for $\partial/\partial x_3$ and the completeness relation equation (10) are used. The summation of $\mathbf{l}$ in eq.(49) is over $l_i = 0...2^{j_i-1}$.

To simplify eq.(49), we define the following matrices

$$\gamma^{a,b}_{\mathbf{j},\mathbf{l},\mathbf{l}'} = \int \phi_{\mathbf{j},\mathbf{l}}(\mathbf{x}) A^a B^b \phi_{\mathbf{j},\mathbf{l}'}(\mathbf{x}) d\mathbf{x}, \tag{50}$$

where the differential operators A and B are

$$A = e^{\frac{1}{2}(\sigma_{\mathbf{j}}^{v_3}/H)^2\left(\frac{\partial}{\partial x_3}\right)^2}, \quad B = \nabla^{-2}\frac{\partial^2}{\partial x_3^2}. \tag{51}$$

Obviously $\gamma^{a,b}_{\mathbf{j},\mathbf{l},\mathbf{l}'}$ depends on $\Delta\mathbf{l} = (|l_1 - l_1'|, |l_2 - l_2'|, |l_3 - l_3'|)$, not $\mathbf{l}$ or $\mathbf{l}'$ individually. Appendix A provides the algorithms to calculate $\gamma^{a,b}_{\mathbf{j},\mathbf{l},\mathbf{l}'}$.

Thus, eq.(49) becomes

$$\epsilon^S_{\mathbf{j},\mathbf{l}} = -\sqrt{\frac{L_1 L_2 L_3}{2^{j_1+j_2+j_3}}} + \sqrt{\frac{L_1 L_2 L_3}{2^{j_1+j_2+j_3}}} \sum_{\mathbf{l}'} \gamma^{1,0}_{\mathbf{j},\mathbf{l},\mathbf{l}'} + \sum_{\mathbf{l}'} \gamma^{1,0}_{\mathbf{j},\mathbf{l},\mathbf{l}'} \epsilon_{\mathbf{j},\mathbf{l}'} + \beta \sum_{\mathbf{l}'} \gamma^{1,1}_{\mathbf{j},\mathbf{l},\mathbf{l}'} \epsilon_{\mathbf{j},\mathbf{l}'} \tag{52}$$

Using the so-called "partition of unity" (Fang & Feng 2000), one can show that

$$\sum_{\mathbf{l}'} \gamma^{1,0}_{\mathbf{j},\mathbf{l},\mathbf{l}'} \simeq 1. \tag{53}$$

Therefore, eq.(52) gives

$$\epsilon^S_{\mathbf{j},\mathbf{l}} \simeq \sum_{\mathbf{l}'} (\gamma^{1,0}_{\mathbf{j},\mathbf{l},\mathbf{l}'} + \beta\gamma^{1,1}_{\mathbf{j},\mathbf{l},\mathbf{l}'}) \epsilon_{\mathbf{j},\mathbf{l}'}. \tag{54}$$

This is the mapping of one-point variables between real and redshift spaces.

4.3. Redshift distortion of the 2nd moment

The second moment of one-point statistics in redshift space is

$$\langle |\epsilon^S_{\mathbf{j},\mathbf{l}}|^2 \rangle \simeq \Big\langle [\sum_{\mathbf{l}'} (\gamma^{1,0}_{\mathbf{j},\mathbf{l},\mathbf{l}'} + \beta\gamma^{1,1}_{\mathbf{j},\mathbf{l},\mathbf{l}'}) \epsilon_{\mathbf{j},\mathbf{l}'}][\sum_{\mathbf{l}''} (\gamma^{1,0}_{\mathbf{j},\mathbf{l},\mathbf{l}''} + \beta\gamma^{1,1}_{\mathbf{j},\mathbf{l},\mathbf{l}''}) \epsilon_{\mathbf{j},\mathbf{l}''}] \Big\rangle. \tag{55}$$

One can show that, even for a weakly non-linear field, both $\langle \epsilon_{\mathbf{j},\mathbf{l}} \epsilon_{\mathbf{j},\mathbf{l}'} \rangle$ and $\gamma^{a,b}_{\mathbf{j},\mathbf{l},\mathbf{l}'}$ are symmetric and quasi-diagonalized with respect to $\mathbf{l}$ and $\mathbf{l}'$, and $\langle |\epsilon_{\mathbf{j},\mathbf{l}}|^2 \rangle$ should be $\mathbf{l}$-independent. The

wavelet counterpart, i.e. $\langle\tilde{\epsilon}_{\mathbf{j},\mathbf{l}}\tilde{\epsilon}_{\mathbf{j},\mathbf{l}'}\rangle \simeq \delta^K_{\mathbf{l},\mathbf{l}'}\langle\tilde{\epsilon}^2_{\mathbf{j},\mathbf{l}}\rangle$, has been shown by Pando, Feng & Fang (2001). Thus, eq.(55) becomes

$$\langle|\epsilon^S_{\mathbf{j},\mathbf{l}}|^2\rangle \simeq \left(\sum_{\mathbf{l}'}\gamma^{1,0}_{\mathbf{j},\mathbf{l},\mathbf{l}'}\gamma^{1,0}_{\mathbf{j},\mathbf{l},\mathbf{l}'} + 2\beta\sum_{\mathbf{l}'}\gamma^{1,0}_{\mathbf{j},\mathbf{l},\mathbf{l}'}\gamma^{1,1}_{\mathbf{j},\mathbf{l},\mathbf{l}'} + \beta^2\sum_{\mathbf{l}'}\gamma^{1,1}_{\mathbf{j},\mathbf{l},\mathbf{l}'}\gamma^{1,1}_{\mathbf{j},\mathbf{l},\mathbf{l}'}\right)\langle|\epsilon_{\mathbf{j},\mathbf{l}}|^2\rangle. \tag{56}$$

Using the completeness relation equation (10), we have

$$\sum_{\mathbf{l}''}\gamma^{a_1,b_1}_{\mathbf{j},\mathbf{l},\mathbf{l}''}\gamma^{a_2,b_2}_{\mathbf{j},\mathbf{l}'',\mathbf{l}'} = \gamma^{a_1+a_2,b_1+b_2}_{\mathbf{j},\mathbf{l},\mathbf{l}'}. \tag{57}$$

Thus, eq.(56) gives

$$\langle|\epsilon^S_{\mathbf{j},\mathbf{l}}|^2\rangle \simeq (\gamma^{2,0}_{\mathbf{j},\mathbf{0},\mathbf{0}} + 2\beta\gamma^{2,1}_{\mathbf{j},\mathbf{0},\mathbf{0}} + \beta^2\gamma^{2,2}_{\mathbf{j},\mathbf{0},\mathbf{0}})\langle|\epsilon_{\mathbf{j},\mathbf{l}}|^2\rangle, \tag{58}$$

where we have used $\gamma^{a,b}_{\mathbf{j},\mathbf{l},\mathbf{l}} = \gamma^{a,b}_{\mathbf{j},\mathbf{0},\mathbf{0}}$. Therefore, we have finally the mapping of $D_\mathbf{j}$ between real and redshift spaces

$$D^S_\mathbf{j} \simeq (\gamma^{2,0}_{\mathbf{j},\mathbf{0},\mathbf{0}} + 2\beta\gamma^{2,1}_{\mathbf{j},\mathbf{0},\mathbf{0}} + \beta^2\gamma^{2,2}_{\mathbf{j},\mathbf{0},\mathbf{0}})D_\mathbf{j}. \tag{59}$$

4.4. Effect of selection functions

In linear approximation, it is reasonable to estimate the effect of redshift distortion of $n^S(\mathbf{s})$ and $\bar{n}^S(\mathbf{s})$ separately. In this case, one can still use eq.(54) as the mapping from $\epsilon^S_{\mathbf{j},\mathbf{l}}$ to $\epsilon_{\mathbf{j},\mathbf{l}}$. We only need to study the effect of the mapping between $\bar{n}^S(\mathbf{s})$ and $\bar{n}(\mathbf{x})$, which is given by

$$\langle\bar{n}^S(\mathbf{s})\rangle_v = \langle\bar{n}[\mathbf{x} + \hat{\mathbf{r}}v_r(\mathbf{x})/H]\rangle_v \simeq \bar{n}(\mathbf{x}) + \frac{1}{H}V_r(\mathbf{x})\hat{\mathbf{r}}\cdot\nabla n^g(\mathbf{x}), \tag{60}$$

where we have used $\langle v_r\rangle_v = V_r$. With the plane-parallel approximation of selection function (§3.2), eq.(60) becomes

$$\bar{n}^S(\mathbf{s}) = \bar{n}(x_3) + \frac{1}{H}\frac{d\bar{n}(x_3)}{dx_3}V_3(\mathbf{x}), \tag{61}$$

where we have dropped $\langle...\rangle_v$ for $\bar{n}^S(\mathbf{s})$. ¿From equation (41), V_3 can be represented by $\delta(\mathbf{x})$, so we have

$$\begin{aligned}\bar{n}^S(\mathbf{s}) &= \bar{n}(x_3)\left[1 - \beta\frac{d\ln\bar{n}(x_3)}{dx_3}\frac{\partial}{\partial x_3}\nabla^{-2}\delta(\mathbf{x})\right] \\ &\simeq \bar{n}(x_3)\left\{1 - \beta\frac{d\ln\bar{n}(x_3)}{dx_3}\frac{\partial}{\partial x_3}\nabla^{-2}\left[\frac{n^g(\mathbf{x})}{\bar{n}(x_3)} - 1\right]\right\}.\end{aligned} \tag{62}$$

Combining eqs.(54) and (62), we have finally

$$\frac{\epsilon^S_{\mathbf{j},\mathbf{l}}}{\bar{n}^S_{\mathbf{j},\mathbf{l}}} \simeq \sum_{\mathbf{l}'}[\gamma^{0,1}_{\mathbf{l},\mathbf{l}'} + \beta\gamma^{1,1}_{\mathbf{l},\mathbf{l}'}]\frac{\epsilon_{\mathbf{j},\mathbf{l}'}}{\bar{n}_{\mathbf{j},\mathbf{l}'}} + \beta\frac{d\ln\bar{n}(x_3)}{dx_3}\bigg|_{\mathbf{j},\mathbf{l}}\sum_{l_3}Q_{\mathbf{j},\mathbf{l},\mathbf{l}'}\frac{\epsilon_{\mathbf{j},\mathbf{l}'}}{\bar{n}_{\mathbf{j},\mathbf{l}'}}, \tag{63}$$

where $d\ln\bar{n}^S(x_3)/dx_3|_{\mathbf{j},\mathbf{l}}$ stands for the mean value of $d\ln\bar{n}^S(x_3)/dx_3$ in the cell $(\mathbf{j},\mathbf{l})$, and $\bar{n}_{\mathbf{j},\mathbf{l}}$ is given by eq.(31). In the last term of eq.(63), $l_1 = l_1'$ and $l_2 = l_2'$, and the summation runs only over l_3. The coefficient $Q_{\mathbf{j},\mathbf{l},\mathbf{l}'}$ is defined by

$$Q_{\mathbf{j},\mathbf{l},\mathbf{l}'} = \int \phi_{\mathbf{j},l_1,l_2,l_3}(\mathbf{x})\frac{\partial}{\partial x_3}\nabla^{-2}\phi_{\mathbf{j},l_1,l_2,l_3'}(\mathbf{x})d\mathbf{x}. \tag{64}$$

The calculation of $Q_{\mathbf{j},\mathbf{l},\mathbf{l}'}$ is given in Appendix A.

Because all $\mathbf{l}$-diagonal elements of $Q_{\mathbf{j},\mathbf{l},\mathbf{l}'}$ are zero (Appendix A), and $\gamma^{a,b}_{\mathbf{j},\mathbf{l},\mathbf{l}'}$ are quasi-$\mathbf{l}$-diagonal, the first and the second terms on the r.h.s. of equation (63) are not correlated. We have then

$$\left\langle\left(\frac{\epsilon^S_{\mathbf{j},\mathbf{l}}}{\bar{n}^S_{\mathbf{j},\mathbf{l}}}\right)^2\right\rangle = (\gamma^{0,2}_{\mathbf{j},\mathbf{0},\mathbf{0}} + 2\beta\gamma^{1,2}_{\mathbf{j},\mathbf{0},\mathbf{0}} + \beta^2\gamma^{2,2}_{\mathbf{j},\mathbf{0},\mathbf{0}})\left\langle\left(\frac{\epsilon_{\mathbf{j},\mathbf{l}}}{\bar{n}_{\mathbf{j},\mathbf{l}}}\right)^2\right\rangle + \left[\beta\frac{d\ln\bar{n}(x_3)}{dx_3}\bigg|_{\mathbf{j},\mathbf{l}}\right]^2\sum_{\mathbf{l}'}Q^2_{\mathbf{l},\mathbf{l}'}\left\langle\left(\frac{\epsilon_{\mathbf{j},\mathbf{l}'}}{\bar{n}_{\mathbf{j},\mathbf{l}'}}\right)^2\right\rangle. \tag{65}$$

For a uniform field, $\langle|\epsilon^S_{\mathbf{j},\mathbf{l}}/\bar{n}^S_{\mathbf{j},\mathbf{l}}|^2\rangle$ and $\langle|\epsilon_{\mathbf{j},\mathbf{l}}/\bar{n}_{\mathbf{j},\mathbf{l}}|^2\rangle$ are $\mathbf{l}$-independent. Thus, equation (65) gives

$$D^S_{\mathbf{j}} = \left(\gamma^{0,2}_{\mathbf{j},\mathbf{0},\mathbf{0}} + 2\beta\gamma^{1,2}_{\mathbf{j},\mathbf{0},\mathbf{0}} + \beta^2\gamma^{2,2}_{\mathbf{j},\mathbf{0},\mathbf{0}} + \left[\beta\frac{d\ln\bar{n}(x_3)}{dx_3}\bigg|_{\mathbf{j},\mathbf{l}}\right]^2\sum_{\mathbf{l}'}Q^2_{\mathbf{0},\mathbf{l}'}\right)D_{\mathbf{j}}. \tag{66}$$

Using the inequality equation (A16), we can show that if

$$\frac{d\ln\bar{n}(x_3)}{dx_3} < \frac{2^{j_3}}{(2\pi)^{3/2}L_3}, \tag{67}$$

we have

$$\left[\beta\frac{d\ln\bar{n}(x_3)}{dx_3}\bigg|_{\mathbf{j},\mathbf{l}}\right]^2\sum_{l_3-l_3'}Q^2_{\mathbf{j},l_3-l_3'} < \beta^2S^2_{\mathbf{j}}. \tag{68}$$

That is, the selection function term in equation (66) is even less than the second order terms $\beta^2S^2_{\mathbf{j}}$ if the selection function is slowly varying with x_3.

5. Testing the DWT mapping between real and redshift spaces

5.1. Simulation samples

We use N-body simulation samples to test the DWT algorithms for recovering the one-point statistics from redshift space to real space. The model parameters are listed in Table

1. Notice that the simulation boxes are relatively large to minimize the effect on the bulk velocities due to the missing power at long wavelengths (Tormen & Bertschinger 1996).

We use a modified P^{3}M code (Jing & Fang 1994) to evolve 128^3 (256^3 for LCDM2) cold dark matter (CDM) particles in a periodic cube of length L on each side. The linear power spectrum is given by the fitting formula in Bardeen et al. (1986). Zel'dovich approximation is applied to set up the initial perturbation. The particles evolve 600 (800 for LCDM2) integration steps from $z_i = 12$ down to $z = 0$ for all the models.

In addition to β at $z \simeq 0$, we can also test the redshift distortion algorithms at high redshifts. In this case, β is a function of z, Ω and Λ as (Lahav et al. 1991)

$$\beta(z, \Omega, \Lambda) \simeq \left[\frac{\Omega(1+z)^3}{\Omega(1+z)^3 + (1-\Omega-\Lambda)(1+z)^2 + \Lambda}\right]^{0.6}. \tag{69}$$

The simulation code is modified to generate light-cone outputs from $z = 3$ to 0 by a similar method in the *Hubble Volume Simulations* (Evrard et al. 2001). Instead of producing spherical light-cones, we apply the plane-parallel approximation in which a plane (light-front) sweeps through the simulation box at the speed of light. Let the LOS be along the x_3-axis, and the position of the light plane at time t be $x_3^L(t)$. The position and velocity of a particle is recorded when it crosses the plane, i.e. when the position $x_3(t)$ of the particles satisfies

$$x_3(t) = x_3^L(t). \tag{70}$$

Since the time step Δt in the simulations is finite, it is computationally impractical to use eq.(70) directly. The position of the plane in time interval from step i to step $i+1$ is approximately

$$x_3^L(t_i + \alpha\Delta t) \simeq x_3^L(t_i) + \alpha[x_3^L(t_{i+1}) - x_3^L(t_i)], \tag{71}$$

where α is from 0 to 1. On the other hand, for a particle we have $x_3(t_i + \alpha\Delta t) \simeq x_3(t_i) + \alpha\Delta t\ v_3(t_i)$, where $v_3(t_i)$ is the velocity of the particle along the LOS. Thus, if we can find a

Table 1

Model	L/h^{-1}Mpc	Ω	Λ	Γ	σ_8	run	particle
LCDM1	800	0.3	0.7	0.225	0.95	6	128^3
LCDM2	800	0.3	0.7	0.21	0.81	1	256^3
OCDM	800	0.3	0.0	0.225	0.95	6	128^3
SCDM	800	1.0	0.0	0.50	0.62	6	128^3
TCDM	800	1.0	0.0	0.25	0.60	6	128^3

Table 1: Models of N-body simulations.

solution of $|\alpha| < 1$ from the following equation

$$x_3(t_i) + \alpha\Delta t\ v_3(t_i) = x_3^L(t_i) + \alpha[x_3^L(t_{i+1}) - x_3^L(t_i)], \tag{72}$$

we have $x_3(t_i + \alpha\Delta t) \simeq x_3^L(t_i + \alpha\Delta t)$, i.e. the particle crosses the plane at time $t_i + \alpha\Delta t$. We then record its position $\mathbf{x}(t_i) + \alpha\Delta t\ \mathbf{v}(t_i)$ and velocity $\mathbf{v}(t_i)$. The accuracy is satisfactory. For example, the difference between $x_3(t_i + \alpha\Delta t)$ and $x_3^L(t_i + \alpha\Delta t)$ is typically less than 50 h^{-1}kpc out to redshift $z = 2.5$ in the LCDM1 model. In the actual simulations, the integration variable is a, the cosmic expansion factor, instead of t.

Since the size of the simulation box is less than the distance swept by the plane from redshift $z = 3$ to 0, the motion of the plane is realized by periodic extensions of the simulation box when the plane meets the boundary. This treatment should not have significant effects on our analyses, because the simulations already impose a periodic boundary condition, and the largest scale analyzed for each simulation is only a quarter of its box size. Once the real-space light-cone output is obtained, the observed redshift of a particle is given by $z_{obs} = z + (1 + z)v_r/c$, where z is the actual redshift, and v_r is the peculiar velocity. To avoid negative z_{obs} caused by peculiar velocities at low redshifts, a lower cut is set to $z = 0.005$. This results in less than a hundred particles bearing a negative z_{obs} in each run, which are then removed from the samples. Three light-cone outputs along the three orthogonal axes are produced for each simulation, which effectively increases the number of realizations by a factor of 3.

5.2. Calculation of $\gamma^{0,1}_{\mathbf{j},\mathbf{0},\mathbf{0}}$, $\gamma^{0,2}_{\mathbf{j},\mathbf{0},\mathbf{0}}$, and $\gamma^{2,0}_{\mathbf{j},\mathbf{0},\mathbf{0}}$

Before testing the theory of recovering $D_{\mathbf{j}}$ (eq.(59)), we need to study the factors $\gamma^{0,1}_{\mathbf{j},\mathbf{0},\mathbf{0}}$, $\gamma^{0,2}_{\mathbf{j},\mathbf{0},\mathbf{0}}$, and $\gamma^{2,0}_{\mathbf{j},\mathbf{0},\mathbf{0}}$, because the first two are the key of the redshift distortion of bulk velocity, while the last one the distortion of velocity dispersion. Below we drop $(\mathbf{0},\mathbf{0})$ in subscripts for simplicity.

By the definition of eq.(50), the factors $\gamma^{0,1}_{\mathbf{j}}$ and $\gamma^{0,2}_{\mathbf{j}}$ are given by

$$\begin{aligned}\gamma^{0,1}_{\mathbf{j}} &= \int \phi_{\mathbf{j},\mathbf{0}}(\mathbf{x})\nabla^{-2}\frac{\partial^2}{\partial x_3^2}\phi_{\mathbf{j},\mathbf{0}}(\mathbf{x})d\mathbf{x}, \\ \gamma^{0,2}_{\mathbf{j}} &= \int \phi_{\mathbf{j},\mathbf{0}}(\mathbf{x})\nabla^{-4}\frac{\partial^4}{\partial x_3^4}\phi_{\mathbf{j},\mathbf{0}}(\mathbf{x})d\mathbf{x}.\end{aligned} \tag{73}$$

We plot $\gamma^{0,1}_{\mathbf{j}}$ and $\gamma^{0,2}_{\mathbf{j}}$ in Fig. 2 for the D4 wavelet. It should be pointed out that $\gamma^{0,b}_{\mathbf{j}}$ depends only on the *shape*, not the scale $\mathbf{j}$ of the scaling function. For instance, $\gamma^{0,1}_{2,2,3} = \gamma^{0,1}_{3,3,4} = \ldots = \gamma^{0,1}_{5,5,6}$, because the 3-D cells of $\mathbf{j} = (2,2,3), (3,3,4)\ldots, (5,5,6)$ have the same shape, i.e. all

the ratios of length : width : height of these cells are 2:2:1, even though they have different volumes (scales). For cubic cells, i.e. $j_1 = j_2 = j_3 = j$, we have $\gamma^{0,1}_{j,j,j} \simeq 1/3$, and $\gamma^{0,2}_{j,j,j} \simeq 1/5$.

The factor $\gamma^{2,0}_{\mathbf{j}}$ is given by

$$\gamma^{2,0}_{\mathbf{j}} = \int \phi_{\mathbf{j},\mathbf{0}}(\mathbf{x}) e^{(\sigma^{v_3}_{\mathbf{j}}/H)^2 \left(\frac{\partial}{\partial x_3}\right)^2} \phi_{\mathbf{j},\mathbf{0}}(\mathbf{x}) d\mathbf{x}. \tag{74}$$

It depends on both the scaling function and the velocity dispersion $\sigma^{v_3}_{\mathbf{j}}$, and therefore it is model-dependent.

The velocity variance $\sigma^{v_3}_{\mathbf{j}}$ is scale-dependent. It is shown in Fig. 3 for all the models, which is similar to Fig. 6 in Yang et al. (2002). Actually, $\sigma^{v_3}_{\mathbf{j}}$ is given by all the power of pairwise velocity on scales less than the scale of $\mathbf{j}$, and therefore, it is larger on larger scales.

To avoid crowding the figure, we only show $\gamma^{2,0}_{j,j,j_3}$ for LCDM1 in Fig. 4. Other modes, such as $\gamma^{2,0}_{j_1,j_2,j_3}$, follow $\gamma^{2,0}_{j,j,j_3}$ closely. An interesting feature seen in Fig. 4 is that $\gamma^{2,0}_{j,j,2}$ and $\gamma^{2,0}_{j,j,3}$ are almost equal to 1 from $j = 2$ to 6, which corresponds to spatial scales from 200 to 12.5 h^{-1} Mpc on the celestial sphere, and 200 to 100 h^{-1} Mpc along the LOS. Even for $\gamma^{2,0}_{j,j,4}$, the dependence on j is only mild. Moreover, this property is model-independent, i.e. for other models, we also have the j-independence of $\gamma^{2,0}_{j,j,2}$ and $\gamma^{2,0}_{j,j,3}$.

The factor $\gamma^{2,0}_{j_1,j_2,j_3}$ is sensitive to $\sigma^{v_3}_{\mathbf{j}}$ (as a variable) when the scale along the LOS is small, but insensitive when the scale is large. For example, when $\sigma^{v_3}_{\mathbf{j}}$ varies from 0 to 500 km s^{-1}, $\gamma^{2,0}_{j,j,3}$ drops from 1 to 0.97, i.e. the change is only 3%, while $\gamma^{2,0}_{j,j,6}$ from 1 to 0.46, i.e. the change is by a factor of 2. If we try to use a scale-independent σ^v to recover the real space power spectrum, we should chose σ^v to give a good fitting on small scales, because the value of σ^v does not significantly affect the large scales.

In addition to j_3, $\gamma^{2,0}_{\mathbf{j}}$ depends on j_1 and j_2 (collectively $j_\perp$) through $\sigma^{v_3}_{\mathbf{j}}$, which is less than 500 km s^{-1} (Fig. 3). Therefore, when the LOS scale is above 100 h^{-1} Mpc, $\gamma^{2,0}_{\mathbf{j}}$ is almost a constant with respect to $j_\perp$. On the other hand, when the scale is below 50 h^{-1} Mpc, $\gamma^{2,0}_{\mathbf{j}}$ shows a mild dependence on $j_\perp$ due to the scale dependence of $\sigma^{v_3}_{\mathbf{j}}$.

In a word, we benefit from the DWT representation to see the different behavior of the two types of the redshift distortion. The former is sensitive to the shape of the mode, not the scale, while the latter just the contrary.

5.3. Recovery of $D_{\mathbf{j}}$

We neglect the effect of selection function here for the simulation samples, which is similar to that on the DWT power spectrum tested in Yang et al. (2002). Since the matrix

$\gamma^{a,b}_{\mathbf{j},\mathbf{l},\mathbf{l}'}$ is quasi-diagonalized with respect to $(\mathbf{l},\mathbf{l}')$, we have approximately $\gamma^{a,b}_{\mathbf{j}} \simeq \gamma^{a,0}_{\mathbf{j}}\gamma^{0,b}_{\mathbf{j}}$. Thus, eq.(59) yields

$$D^S_{\mathbf{j}} \simeq \gamma^{2,0}_{\mathbf{j}}(1 + 2\beta\gamma^{0,1}_{\mathbf{j}} + \beta^2\gamma^{0,2}_{\mathbf{j}})D_{\mathbf{j}}. \tag{75}$$

In eq.(75), the contributions of the operators A and B to the redshift distortion are separated. Usually terms of B ($\gamma^{0,1}_{\mathbf{j}}$ and $\gamma^{0,2}_{\mathbf{j}}$) are called linear redshift distortion, and that of A ($\gamma^{2,0}_{\mathbf{j}}$) non-linear distortion. These terminologies may cause a confusion. Here "linear" means only that B is from the linear term of V_3 in the approximation eq.(48), and "non-linear" means that A is non-linear of the velocity dispersion σ^{v_3}. It does not imply that the terms of B is enough for estimating the redshift distortion of a field that is in the linear regime. Since the velocity dispersion σ^v is non-zero in the linear regime, the non-linear distortion term of A may also play a non-negligible role even when the field is linear. In this paper, we follow the tradition to call the terms of B and A the linear and non-linear effects of redshift distortion, respectively. However, it should be kept in mind that these names do not reflect whether the field is linear or non-linear.

For $\mathbf{j}$-diagonal modes, equation (75) reduces to $D^S_{\mathbf{j}} \simeq \gamma^{2,0}_{\mathbf{j}}(1 + 2/3\beta + 1/5\beta^2)D_{\mathbf{j}}$. The factors within the parentheses are known as the linear redshift-to-real space mapping for two-point correlation function (Kaiser 1987).

Figure 5 shows the recovery of $\mathbf{j}$-diagonal $D_{\mathbf{j}}$. It is evident that the recovery equation (75) works very well on all scales and redshifts considered, except for the SCDM model at $z = 0.71$. Due to greater β parameters, the distortions of the TCDM and the SCDM models are generally stronger than that of the rest. For these two models, $D^S_{\mathbf{j}}$ is almost parallel to $D_{\mathbf{j}}$, which indicates a very weak non-linear redshift distortion on all scales. This is consistent with the fact that the velocity dispersions of the two models are small on all scales compared to the others. Since the volume of a cubic cell with $12.5\mathrm{h}^{-1}$Mpc on each side is approximately the same as that of a sphere with a radius of $8\mathrm{h}^{-1}$Mpc, the values of $D_{6,6,6}$ are consistent with σ^2_8 at corresponding redshifts for each model. The differences, nevertheless, are due to the difference in the window functions.

Similar to $D_{\mathbf{j}}$, one can generalize σ_8 to σ_R, which is the *rms* density fluctuation in a sphere of radius R. Since the behavior of σ^2_R is the same as $D_{j,j,j}$, one can recover the real space σ_R from the redshift space σ^S_R in a similar way as eq.(75), i.e. $\sigma^S_R \simeq [\gamma^{2,0}_{j,j,j}(1 + 2/3\beta + 1/5\beta^2)]^{1/2}\sigma_R$, where j is chosen to match the volumes of the DWT cell and the spherical top-hat window of radius R. Figure 6 demonstrates the recovery of σ_R for all the models. It is a coincidence that $\sigma^S_8 \simeq \sigma_8$ for the low density models.

Figures 7 and 8 give the recovery of off-diagonal $D_{\mathbf{j}}$. This recovery works well on scales above 50 h^{-1} Mpc. On scales less than 50 h^{-1} Mpc, the error is noticeable but still small. This is partially due to the approximation of the quasi-diagonality of the covariance

$\langle \epsilon_{\mathbf{j},\mathbf{l}} \epsilon_{\mathbf{j},\mathbf{l}'} \rangle \simeq \delta^K_{\mathbf{l},\mathbf{l}'} \langle \epsilon^2_{\mathbf{j},\mathbf{l}} \rangle$ in equation (56). Moreover, the separation between the factors involving operators A and B in eq.(75) is not perfect as well.

The errors of recovering $D_{\mathbf{j}}$ can be more clearly seen via a comparison with the recovery of the DWT power spectrum from redshift space $P^S_{\mathbf{j}}$ to real space $P_{\mathbf{j}}$. It is (Yang et al. 2002)

$$P^S_{\mathbf{j}} \simeq \Gamma^{2,0}_{\mathbf{j}} (1 + 2\beta \Gamma^{0,1}_{\mathbf{j}} + \beta^2 \Gamma^{0,2}_{\mathbf{j}}) P_{\mathbf{j}}, \tag{76}$$

where $\Gamma^{a,b}_{\mathbf{j}}$ is defined by eq.(50) but with replacement of $\phi_{\mathbf{j}}$ to $\psi_{\mathbf{j}}$. The factors $\Gamma^{0,1}_{\mathbf{j}}$ and $\Gamma^{0,2}_{\mathbf{j}}$ also satisfy $\Gamma^{0,1}_{j,j,j} \simeq 1/3$ and $\Gamma^{0,2}_{j,j,j} \simeq 1/5$. The non-linear term $\Gamma^{2,0}_{\mathbf{j}}$ behaves the same as $\gamma^{2,0}_{\mathbf{j}}$, but with a little stronger dependence on $\mathbf{j}$.

We find that the recovery of $D_{\mathbf{j}}$ by eq.(75) has an error within 10% in most cases, while the DWT power spectrum recovery eq.(76) is accurate to 5% or better. This is because that the quasi-diagonality of the SFC's covariance $\langle \epsilon_{\mathbf{j},\mathbf{l}} \epsilon_{\mathbf{j},\mathbf{l}'} \rangle \simeq \delta^K_{\mathbf{l},\mathbf{l}'} \langle \epsilon^2_{\mathbf{j},\mathbf{l}} \rangle$ is poorer than the quasi-diagonality of the WFC's covariance $\langle \tilde{\epsilon}_{\mathbf{j},\mathbf{l}} \tilde{\epsilon}_{\mathbf{j},\mathbf{l}'} \rangle \simeq \delta^K_{\mathbf{l},\mathbf{l}'} \langle \tilde{\epsilon}^2_{\mathbf{j},\mathbf{l}} \rangle$. As we know from the DWT analysis, the covariance $\langle \tilde{\epsilon}_{\mathbf{j},\mathbf{l}} \tilde{\epsilon}_{\mathbf{j},\mathbf{l}'} \rangle$ is always quasi-diagonal for a Gaussian field, regardless the power spectrum[3]. On the other hand, the quasi-diagonality of the covariance $\langle \epsilon_{\mathbf{j},\mathbf{l}} \epsilon_{\mathbf{j},\mathbf{l}'} \rangle$ is not a generic mathematical property, but only an approximation.

5.4. Problems with real samples

All the above algorithms can be applied to real samples as well. However, there are several problems to be considered in the analysis on real data.

1. Data assignment on grid

To calculate the moments of counts-in-cells, one has to cast a grid on the data set either explicitly or implicitly, and assign the data in cells defined by the grid. The arbitrariness of the assignment may lead to significant error (Colombi, Bouchet & Schaeffer 1995). One way to reduce this error is to shift the grid. It is well known that this assignment may also result in spurious features of the power spectrum on scales around the Nyquist frequency of the grid. In the DWT analysis, one can use different grids, but no shift is needed. For a given grid, the assignment is realized by the same scaling function used for the data decomposition. Since scaling functions are orthogonal and complete in each given scale $\mathbf{j}$, the spurious features and false correlations can be completely avoided (Fang & Feng 2000). To test the effect of the assignment on the one point statistics, we calculate $D_{j,j,j}$ for a snapshot sample of

[3]This is the property employed for data compression of the DWT analysis (Louis, Maass and Rieder 1997)

LCDM1 with randomly shifted grids. The snapshot sample is take at $z = 0.11$. In Fig. 9, Snap-0 represents $D_{j,j,j}$ without grid shifting, while Snap-32 and Snap-1024, respectively, the average over 32, and 1024 random shifts for grids on all scales. No significant deviation is detected among the results.

2. Boundary condition and edge effect

In a real survey, the edge effect is unavoidable due to the geometry (e.g. Szapudi & Colombi 1996). Since the DWT bases are localized in physical space, the effect of edges can be effectively suppressed by dropping modes that are close to the boundary of the samples. In other words, when calculating $D_{\mathbf{j}}$, the averaging in eq.(17) runs only over modes that are not significantly affected by the edge effect, and the normalization factor $L_1 L_2 L_3$ is replaced by the volume over which the average takes place. This method has been tested numerically in the power spectrum detection (Pando & Fang 1998b). It shows that the power spectrum can be fairly reconstructed regardless whether applying a periodic boundary or zero padding outside of the samples. The treatment of dropping edge modes has also been successfully employed to obtain the power spectrum for the Las Campanas redshift survey of galaxies, which has a slice-like geometry (Yang et al. 2001b). When the interested scale is close to the dimension of the sample, one cannot afford to drop all the edge modes, and then a more thorough treatment is needed. The edge effect exists in our simulation sample because the light-cone output is not periodic along the redshift axis, while we have used periodic D4 wavelets in the analysis. For comparison, the real-space light-cone $D_{j,j,j}$ from Fig. 5 is included in Fig. 9. There is no significant difference between the results from the snapshot, which is truly periodic, and that from the light-cone around the same redshift. The slightly larger standard deviation of the light-cone result at 200 h^{-1}Mpc (a quarter of the simulation box) is due to a larger fraction of edge cells.

3. Non-Poisson sampling

In §3.3, we have considered the correction for Poisson sampling. It is sufficient for simulation samples. However, it may not be typical for real samples. For instance, some galaxy catalogs may be given by sub-Poisson sampling on small scales, or small halos (e.g. Bullock, Wechsler & Somerville, 2002). The sub-Poisson distribution is simply due to very low mass of the considered halo, so that it cannot host any additional objects. In other words, the sub-Poisson distribution is significant on small scales on which galaxies are anticorrelated. Therefore, this sub-Poisson sampling is similar to the sub-Poisson distribution of the Fermi-Dirac statistics (one state can host no more than one particle). The effect of this sub-Poisson has been extensively studied in quantum optics (e.g. Martin & Landauer, 1992). It is possible to extend the Poisson sampling eq.(35) to include Fermi-like sampling. The algorithm for a modified Poisson sampling has been developed by Jamkhedkar, Bi and Fang (2001) (see

their Append B).

6. β estimators with the DWT moment of one-point statistics

6.1. β estimator with scale-decomposed quantities

We first consider a β estimator without non-linear effect. For instance, $\gamma^{2,0}_{j,j,2} \simeq \gamma^{2,0}_{j,j,3} \simeq 1$ (Fig. 4), i.e. the non-linear effects are small above 100 h^{-1} Mpc along the LOS, eq.(75) gives

$$D^S_{j_1,j_2,j_3} \simeq (1 + 2\beta\gamma^{0,1}_{j_1,j_2,j_3} + \beta^2\gamma^{0,2}_{j_1,j_2,j_3})D_{j_1,j_2,j_3}, \quad j_3 = 2, 3. \tag{77}$$

It is easy to construct a β estimator with eq.(77), because the quantities $D_{\mathbf{j}}$, $D^S_{\mathbf{j}}$, and $\gamma^{a,b}_{\mathbf{j}}$ are not rotationally invariant, but they satisfy the following symmetries with respect to the triple indices (j_1, j_2, j_3).

1. If the cosmic density and velocity fields are statistically isotropic, $D_{\mathbf{j}}$ in real space is invariant with respect to cyclic permutations of index $\mathbf{j} = (j_1, j_2, j_3)$, i.e.

$$D_{j_1,j_2,j_3} = D_{j_3,j_1,j_2} = D_{j_2,j_3,j_1}. \tag{78}$$

2. In the plane-parallel approximation, i.e. the coordinate x_3 is in the redshift direction, we have

$$D^S_{j_1,j_2,j_3} = D^S_{j_2,j_1,j_3}, \tag{79}$$

$$\gamma^{a,b}_{j_1,j_2,j_3} = \gamma^{a,b}_{j_2,j_1,j_3}. \tag{80}$$

Using eqs.(77)-(80), we have a β estimator as follows

$$\frac{D^S_{j,2,3}}{D^S_{j,3,2}} \simeq \frac{1 + 2\beta\gamma^{0,1}_{j,2,3} + \beta^2\gamma^{0,2}_{j,2,3}}{1 + 2\beta\gamma^{0,1}_{j,3,2} + \beta^2\gamma^{0,2}_{j,3,2}}. \tag{81}$$

Eq.(81) looks very similar to the β estimator with quadrupole-to-monopole ratio, or the multipole moments of two-point correlation function. However, eq.(81) contains not only the information of shape (like multipole moments), but also scales. All the DWT quantities in eq.(77) are on scale $\mathbf{j}$. That is, the β in eq.(77) refers to mode $\mathbf{j} = (j_1, j_2, j_3)$. Therefore, if β is scale-dependent, the β estimated by eq.(81) is its value referring to $\mathbf{j}$. On the other hand, if β is scale-free, the values of β given by estimator eq.(81) with different mode $\mathbf{j}$ should be the same.

Figure 10 plots the results in the case of a scale-free β for the LCDM1 model using estimators with $j = 2, 3, 4$. The results indeed show that the estimated β is independent

of the **j** used in the estimator, and it follows the theoretical curves in the entire redshift range considered. Therefore, we expect that the estimator (81) would be useful to study the scale-dependence of bias parameters of galaxies.

For comparison, fig 11 shows the β estimated from quadrupole-to-monopole ratio as

$$\frac{P_2^S(k)}{P_0^S(k)} = \frac{\frac{4}{3}\beta + \frac{4}{7}\beta^2}{1 + \frac{2}{3}\beta + \frac{1}{5}\beta^2}, \tag{82}$$

where $P_2^S(k)$ and $P_0^S(k)$ are the quadrupole moment and the monopole moment of the power spectrum $P^S(\mathbf{k})$ respectively (Cole, Fisher & Weinberg 1994, hereafter CFW; Hamilton 1997). We average the results from wavelength 50 h^{-1}Mpc to 400 h^{-1}Mpc for each realization. Thus the error bars are among different realizations of each model. As noticed in CFW, this estimator gives a lower β than the true value at $z \simeq 0$ even for wavelengths > 50 h^{-1}Mpc. In addition, we find that it progressively overestimates β at higher and higher redshifts. It is suggested in CFW that the underestimate at short wavelengths is due to the impact of non-linear gravitational clustering. However, this explanation is still difficult to apply for the underestimate at long wavelengths, and the overestimate at high redshift, as cosmic field on long wavelengths or high redshifts should be linear.

This discrepancy occurs because the quadrupole-to-monopole ratio eq.(82) is scale-dependent even when the field is in linear regime. This scale-dependence is given by the non-linear redshift distortion, or the distortion of velocity dispersion. As mentioned in §5.3, σ^{v_3} is non-zero in linear clustering regime, the non-linear redshift distortion (or the distortion of σ^{v_3}) should be considered regardless whether the field is linear or non-linear. Therefore, the discrepancy in CFW cannot be eliminated for long wavelengths or high redshift. To solve this problem, extra information, such as the power-spectrum index of the density fluctuations, or the real-space correlation function, is added in the quadrupole-to-monopole ratio estimator eq.(82) (Peacock et al. 2001).

6.2. β estimator considering with non-linear redshift distortion

Different from the quadrupole-to-monopole ratio, the DWT β estimators are scale-decomposed. It is useful to consider scale-dependent effect. The DWT estimators are able to consider the non-linear redshift distortion (σ^{v_3} redshift distortion) without assuming extra information. Actually, the result with estimator eq.(81) has already shown the effect of the non-linear redshift distortion. We can see from Fig. 10 that the β estimated by eq.(81) are slightly dependent on j, and it is progressively higher in the order $j = 2, 3, 4$. This can be explained with Fig. 4, which shows that the factor $\gamma_{\mathbf{j}}^{2,0}$ is less than one, and is smaller for

a smaller scale. Thus the estimator eq.(81), which ignores the factor $\gamma_{\mathbf{j}}^{2,0}$ in eq.(77), leads to a progressively higher β in the order $j = 2, 3, 4$. Thus, a simplest way to estimate the non-linear effect is to take an average over β given by eq.(81) with different j. The left panel of Figure 12 presents the averaged β from Fig. 10 for the four models. The error bars contain the contribution of the non-linear effect. That is, the DWT algorithm can do a self-test on whether the result is largely affected by the non-linear effect.

More delicate β estimators can be constructed if we consider the following properties: the non-linear factor $\gamma_{\mathbf{j}}^{2,0}$ depends only on j_3, but independent of $j_\perp$ if the LOS scale is above 100 h^{-1}Mpc, while the linear factors $\gamma_{\mathbf{j}}^{0,1}$ and $\gamma_{\mathbf{j}}^{0,2}$ depends only on the shape of the DWT mode (§5.2). These properties apply to $\Gamma_{\mathbf{j}}^{2,0}$, $\Gamma_{\mathbf{j}}^{0,1}$, and $\Gamma_{\mathbf{j}}^{0,2}$ as well. Thus, we can combine modes with similar j_3 but different shapes to cancel the non-linear factors, such as

$$\frac{\Gamma^{2,0}_{j,2,3}\Gamma^{2,0}_{j',3,2}}{\Gamma^{2,0}_{j',2,3}\Gamma^{2,0}_{j,3,2}} \simeq 1, \quad j \neq j'. \tag{83}$$

Thus, from eq.(76), we have a β estimator as

$$\frac{P^S_{j,2,3}P^S_{j',3,2}}{P^S_{j',2,3}P^S_{j,3,2}} = \frac{(1+2\beta\Gamma^{0,1}_{j,2,3}+\beta^2\Gamma^{0,2}_{j,2,3})(1+2\beta\Gamma^{0,1}_{j',3,2}+\beta^2\Gamma^{0,2}_{j',3,2})}{(1+2\beta\Gamma^{0,1}_{j',2,3}+\beta^2\Gamma^{0,2}_{j',2,3})(1+2\beta\Gamma^{0,1}_{j,3,2}+\beta^2\Gamma^{0,2}_{j,3,2})}. \tag{84}$$

This estimator is similar to that in Yang et al. (2002). It can be used for any pairs ($j \neq j'$) even when the scale of j is small. The right panel of Figure 12 shows that for the four models, the β estimated by eq.(84) has no more than about 15% error at all redshifts $z < 3$. One can also use the modes $(j, 3, 4)$, $(j, 4, 3)$ to replace modes $(j, 2, 3)$ and $(j, 3, 2)$ in eqs.(83) and (84), which gives similar results to Fig. 12. That is, the weakly non-linear redshift distortion can be considered by the DWT β estimators on scales until about 50 h^{-1} Mpc when the quadrupole-to-monopole estimator shows significant errors (Fig. 11).

The counterpart of eq.(84) with $D_{\mathbf{j}}$,

$$\frac{D^S_{j,2,3}D^S_{j',3,2}}{D^S_{j',2,3}D^S_{j,3,2}} = \frac{(1+2\beta\gamma^{0,1}_{j,2,3}+\beta^2\gamma^{0,2}_{j,2,3})(1+2\beta\gamma^{0,1}_{j',3,2}+\beta^2\gamma^{0,2}_{j',3,2})}{(1+2\beta\gamma^{0,1}_{j',2,3}+\beta^2\gamma^{0,2}_{j',2,3})(1+2\beta\gamma^{0,1}_{j,3,2}+\beta^2\gamma^{0,2}_{j,3,2})}, \tag{85}$$

is not as good as eq.(84). It causes an error of about 40% in β because again the quasi-diagonality of the SFC's covariance is poorer than that of WFC's. Since a DWT decomposition of a random field yields variables for calculating both the power spectrum and one-point statistics, the β estimations with eqs.(81) and (84) can be done in the same time.

An accurate β estimator requires the knowledge of a precise recovery of $P_{\mathbf{j}}$ or $D_{\mathbf{j}}$, which accounts for the non-linear redshift distortion due to the velocity dispersion, and even the

second order effect of the bulk velocity ignored in eq.(48). In other words, the non-linear redshift distortion exists even on scales that are linear in the sense of structure formation, and it must be corrected to achieve a reliable and accurate β.

7. Discussion and Conclusion

We have developed the one-point statistics of a perturbed density field with the multiresolutional decomposition based on discrete wavelet transform. Since the scale and shape of the DWT bases are well defined, this frame work is very effective to deal with problems of how the one-point distribution and its moments depend on the scale and shape of the window function. With this property, we have established the algorithm of one-point variable and its moments in considering the effects of Poisson sampling and selection function. We have also established the algorithm for recovering the DWT one-point statistics from the redshift distortion due to bulk velocity, velocity dispersion and selection function.

Because the recovery of the real-space DWT one-point variable and its moments can be realized scale-by-scale, one can design β estimators which are sensitive to the scale-dependence of β, for instance, caused by the scale-dependence of bias parameter of galaxies. These β estimators are effective in avoiding the difficulty caused by the scale-dependence of the non-linear redshift distortion. Compared with conventional β estimators (Peacock et al 2001), the DWT β estimators do not need to assume that the velocity dispersion is scale-independent, or to add extra information, such as the power-spectrum index or the real-space correlation function of the field. Numerical tests by N-body simulation samples show that the proposed estimators can yield the correct value of β with about 15% uncertainty for all popular CDM models in the redshift range $z \leq 3$.

Since DWT decomposition contains two sets of bases, the scaling function $\phi_{j,l}(x)$ and wavelet $\psi_{j,l}(x)$, a DWT decomposition of a density field $\delta(x)$ actually yields variables for one-point statistics $\epsilon_{j,l} = \int \phi_{j,l}(x)\delta(x)dx$ as well as the variables for calculating the power spectrum $\tilde{\epsilon}_{j,l} = \int \psi_{j,l}(x)\delta(x)dx$ (Fang & Feng 2000). In this sense, one can say that the DWT decomposition unifies the algorithm of CiC and power spectrum, which are only two aspects of the statistics with the DWT variables SFCs and WFCs respectively. For a finite size sample, these two aspects of statistics can play different roles: the former contains information of the perturbations on scales larger than the size, while the latter does not. However, the latter generally has diagonalized covariance, while the former does not. Therefore, the β estimators with WFCs are better than SFCs, while SFCs are useful to estimate the effect of perturbations on large scales.

Actually, the DWT decomposition can provide more types of statistics variables. For 2-D or 3-D samples, we have variables defined as

$$\int \delta(\mathbf{x})\phi_{j_1,l_1}(x_1)\psi_{j_2,l_2}(x_2)\psi_{j_3,l_3}(x_3)d\mathbf{x}, \tag{86}$$

$$\int \delta(\mathbf{x})\phi_{j_1,l_1}(x_1)\phi_{j_2,l_2}(x_2)\psi_{j_3,l_3}(x_3)d\mathbf{x}. \tag{87}$$

Obviously, these variables are sampled partially by the scaling function $\phi_{j,l}(x)$, and partially by the wavelet $\psi_{j,l}(x)$. Statistics with these variables are not typical CiC, or power spectrum. They are, however, useful to study the one-point statistics, or power spectrum of 2-D and 3-D samples. With the method developed in this paper, it is not difficult to calculate various corrections (Poisson sampling, selection function, redshift distortion) on the one-point statistics with variables (86) or (87).

HZ is grateful to Daniel Eisenstein for extensive discussions on this paper and facilitating the LCDM2 simulation. HZ would also like to thank David Burstein for hosting the utility codes in this paper.

A. Calculations of $\gamma_{\mathbf{j}}^{a,b}$, and $Q_{\mathbf{j},\mathbf{l},\mathbf{l}'}$

A.1. $\gamma_{\mathbf{j}}^{0,b}$

Let us consider the plane-parallel approximation, i.e. coordinate x_3 is in the redshift direction. By definition eq.(50), we have

$$\gamma_{\mathbf{j}}^{0,b} = \int \phi_{\mathbf{j},\mathbf{l}}(\mathbf{x})\frac{\partial^{2b}}{\partial x_3^{2b}}\nabla^{-2b}\phi_{\mathbf{j},\mathbf{l}}(\mathbf{x})d\mathbf{x}. \tag{A1}$$

Because 1-D scaling function $\phi_{j,l}(x)$ is given by dilating and translating the basic wavelet $\phi(\eta)$ as

$$\phi_{j,l}(x) = \left(\frac{2^j}{L}\right)^{1/2}\phi(\frac{2^j x}{L} - l), \tag{A2}$$

the Fourier transform of $\psi_{j,l}(x)$ is

$$\phi_{j,l}(x) = \frac{1}{L}\sum_{n=-\infty}^{\infty}\hat{\phi}_{j,l}(n)e^{-i2\pi nx/L}, \tag{A3}$$

and

$$\hat{\phi}_{j,l}(n) = \left(\frac{L}{2^j}\right)^{1/2}\hat{\phi}(n/2^j)e^{-i2\pi nl/2^j}, \tag{A4}$$

where $\hat{\phi}(n)$ is the Fourier transform of the basic scaling function

$$\hat{\phi}(n) = \int_{-\infty}^{\infty} \phi(\eta) e^{-i2\pi n\eta} d\eta. \tag{A5}$$

The function $|\hat{\phi}_{j,l}(n)|^2$ is shown in Fig. 1.

Thus, equation (A1) becomes

$$\gamma^{0,b}_{j_1,j_2,j_3} = \frac{1}{2^{j_1+j_2+j_3}} \sum_{n_1,n_2,n_3=\infty}^{\infty} \left(\frac{k_3}{k}\right)^{2b} |\hat{\phi}(u_1)\hat{\phi}(u_2)\hat{\phi}(u_3)|^2, \tag{A6}$$

where vector $\mathbf{k} = 2\pi(n_1/L_1, n_2/L_2, n_3/L_3)$, and $\mathbf{u} = (n_1/2^{j_1}, n_2/2^{j_2}, n_3/2^{j_3})$. Since $\hat{\phi}(n)$ is non-zero only around $|n| \lesssim 1$, the summation of equation (A6) actually only over numbers of $|n_i| \lesssim 2^{j_i}$.

If $L_1 = L_2 = L_3 = L$, equation (A6) becomes

$$\gamma^{0,b}_{j_1,j_2,j_3} = \frac{1}{2^{j_1+j_2+j_3}} \sum_{n_1,n_2,n_3=\infty}^{\infty} \left(\frac{n_3}{n}\right)^{2b} |\hat{\phi}(u_1)\hat{\phi}(u_2)\hat{\phi}(u_3)|^2. \tag{A7}$$

A.2. $\gamma^{2,0}_{\mathbf{j}}$

If $\sigma^v(\mathbf{x})$ is independent of $\mathbf{x}$, $\gamma^{2,0}_{\mathbf{j}}$ is

$$\gamma^{2,0}_{j_1,j_2,j_3} = \frac{1}{2^{j_1+j_2+j_3}} \sum_{n_1,n_2,n_3=-\infty}^{\infty} |\hat{\phi}(u_1)\hat{\phi}(u_2)\hat{\phi}(u_3)|^2 \exp[-(\sigma^{v_3}/H)^2(\hat{r}\cdot\mathbf{k})^2]. \tag{A8}$$

In the plane-parallel approximation, we have

$$\gamma^{2,0}_{j_1,j_2,j_3} = \frac{1}{2^{j_3}} \sum_{n_3=-\infty}^{\infty} |\hat{\phi}(u_3)|^2 \exp[-(\sigma^{v_3}k_3/H)^2]. \tag{A9}$$

The summation of equations (A8) and (A9) also runs only over numbers of $|n_i| \lesssim 2^{j_i}$.

A.3. $\gamma^{a,b}_{\mathbf{j},\mathbf{l},\mathbf{l}'}$

Using the results for $\gamma^{0,b}_{\mathbf{j}}$ and $\gamma^{2,0}_{\mathbf{j}}$, it is easy to find

$$\gamma^{a,b}_{\mathbf{j},\mathbf{l},\mathbf{l}'} = \frac{1}{2^{j_1+j_2+j_3}} \sum_{n_1,n_2,n_3=-\infty}^{\infty} \left(\frac{k_3}{k}\right)^{2b} \cos[2\pi\mathbf{u}\cdot(\mathbf{l}'-\mathbf{l})] \exp[-(a/2)(\sigma^{v_3}k_3/H)^2] |\hat{\phi}(u_1)\hat{\phi}(u_2)\hat{\phi}(u_3)|^2. \tag{A10}$$

It is obvious from equation (A10) that $\gamma^{a,b}_{\mathbf{j},\mathbf{l},\mathbf{l}'}$ is symmetric with respect to $\mathbf{l}$ and $\mathbf{l}'$, and it depends only on the difference $(|l_1 - l'_1|, |l_2 - l'_2|, |l_3 - l'_3|)$. Consequently, $\gamma^{a,b}_{\mathbf{j},\mathbf{l},\mathbf{l}}$ is independent of $\mathbf{l}$. In addition, the elements $\gamma^{a,b}_{\mathbf{j},\mathbf{l},\mathbf{l}}$ are dominant over $\gamma^{a,b}_{\mathbf{j},\mathbf{l},\mathbf{l}'}$ with $\mathbf{l} \neq \mathbf{l}'$, because the latter sums over oscillating terms.

A.4. $Q_{\mathbf{j},\mathbf{l},\mathbf{l}'}$

The quantity $Q_{\mathbf{j},\mathbf{l},\mathbf{l}'}$ is given by eq.(64)

$$Q_{\mathbf{j},\mathbf{l},\mathbf{l}'} = \int \phi_{\mathbf{j},l_1,l_2,l_3}(\mathbf{x}) \frac{\partial}{\partial x_3} \nabla^{-2} \phi_{\mathbf{j},l_1,l_2,l'_3}(\mathbf{x}) d\mathbf{x}. \tag{A11}$$

For index $\mathbf{l}, \mathbf{l}'$, It depends only on the difference $l_3 - l'_3$. We have

$$Q_{\mathbf{j},\mathbf{l},\mathbf{l}'} = Q_{\mathbf{j},l_3-l'_3} = \frac{1}{2^{j_1+j_2+j_3}} \sum_{n_1,n_2,n_3=\infty}^{\infty} \frac{k_3}{k^2} \sin[2\pi u_3(l_3 - l'_3)] |\hat{\phi}(u_1)\hat{\phi}(u_2)\hat{\phi}(u_3)|^2. \tag{A12}$$

Equation (A12) gives

$$Q_{\mathbf{j},l_3-l'_3} = 0, \quad \text{if} \quad l_3 - l'_3 = 0. \tag{A13}$$

Since

$$\sum_{l_3-l'_3=0}^{2^{j_3}-1} \sin[2\pi u_3(l_3 - l'_3)] \sin[2\pi u'_3(l_3 - l'_3)] \simeq \begin{cases} 1/2\pi u_3 & \text{if } u_3 = u'_3 \\ 0 & \text{otherwise} \end{cases}, \tag{A14}$$

we have

$$\sum_{l_3-l'_3} Q^2_{\mathbf{j},l_3-l'_3} = \frac{1}{2^{2(j_1+j_2+j_3)}} \frac{1}{2\pi u_3} \sum_{n_1,n_2,n_3=-\infty}^{\infty} \left(\frac{k_3}{k^2}\right)^2 |\hat{\phi}(u_1)\hat{\phi}(u_2)\hat{\phi}(u_3)|^4. \tag{A15}$$

Thus, equations(A7) and (A15) yield

$$\sum_{l_3-l'_3} Q^2_{\mathbf{j},l_3-l'_3} < \left[\frac{(2\pi)^{3/2} L_3}{2^{j_3}}\right]^2 [\gamma^{0,1}_{\mathbf{j}}]^2. \tag{A16}$$

REFERENCES

Alimi, J.M., Blanchard, A. & Schaeffer, R. 1990, ApJ, 349L, 5

Bardeen, J.M., Bond, J.R., Kaiser, N. & Szalay, A.S. 1986, ApJ, 304, 15

Bertschinger, E. & Dekel, A. 1989, ApJ, 336L, 5

Bullock, J.S., Wechsler, R.H. & Somerville, R.S. 2002, MNRAS, 329, 246.

Cole, S., Fisher, K.B. & Weinberg, D.H. 1994, MNRAS, 267, 785

Coles, P. & Jones, B. 1991 MNRAS, 248, 1

Colombi, S., Bouchet, F.R. & Schaeffer, R. 1995, ApJS, 96, 401

Daubechies I. 1992, Ten Lectures on Wavelets, (Philadelphia, SIAM)

Dekel, A., Bertschinger, E. & Faber, S.M. 1990, ApJ, 364, 349

Dekel, A., Eldar, A., Kolatt, T., Yahil, A., Willick, J.A., Faber, S.M., Courteau, S. & Burstein, D. 1999, ApJ, 522, 1

Evrard, A.E., MacFarland, T., Couchman, H.M.P., Colberg, J.M., Yoshida, N., White, S.D.M., Jenkins, A., Frenk, C.S., Pearce, F.R., Efstathiou, G., Peacock, J.A. & Thomas, P.A. 2001, astro-ph/0110246

Fan, Z.H. & Bardeen, J.M. 1995, Phys. Rev. D51, 6714

Fang, L.Z. & Feng, L.L. 2000, ApJ, 539, 5

Fang, L.Z. & Thews, R. 1998, Wavelet in Physics, (World Scientific, Singapore)

Feng, L.L. & Fang, L.Z. 2000, ApJ, 535, 519

Feng, L.L., Pando, J. & Fang, L.Z. 2001, ApJ, 555, 74

Gaztañaga, E. 1992, ApJ, 398L, 17

Gaztañaga, E. & Croft, R.A.C. 1999, MNRAS, 309, 885

Hamilton, A. J. S. 1985, ApJ, 292L, 35

Hamilton, A.J.S. 1997, astro-ph/9708102

Hubble, E. 1934, ApJ, 79, 8

Jamkhedkar, P., Bi, H. G. & Fang, L.Z. 2001, ApJ, 561, 94

Jamkhedkar, P., Zhan, H. & Fang, L.Z. 2000, ApJ, 543L, 1

Jing, Y.P. & Fang, L.Z. 1994, ApJ, 432, 438

Kaiser, N. 1987, MNRAS, 227, 1

Kim, R.S. & Strauss, M.A. 1998, 493, 39

Lahav, O., Rees, M. J., Lilje, P. B. & Primack, J. R. 1991, MNRAS, 251, 128

Louis, A.K., Maass, P. & Rieder, A. 1997, Wavelets: Theory and Application, (John Wiley, New York)

Mallat, S.G. 1989a, IEEE Trans., 11, 674

Mallat, S.G. 1989b, Trans. Am. Math. Soc., 315, 69

Martin, T. & Landauer, 1992, Phys. Rev. B45, 1742

Meiksin, A. & Bouchet, F.R. 1995, ApJ, 448L, 85

Meyer, Y. 1992, Wavelets and Operators (New York: Cambridge Press)

Pando, J. & Fang, L.Z. 1998a, A&A, 340, 335

Pando, J. & Fang, L.Z. 1998b, Phys. Rev. E57, 3593

Pando, J., Feng, L.L. & Fang, L.Z. 2001, ApJ, 554, 841

Pando, J., Feng, L.L., Jamkhedkar, P., Zheng, W., Kirkman, D., Tytler, D. & Fang, L.Z. 2002, ApJin press, astro-ph/0204092

Peacock, J.A. et al. 2001, Nature, 410, 169

Peebles, P.J.E. 1980, The Large Scale Structure of the Universe (Princeton: Princeton Univ. Press)

Szapudi, I. & Colombi, S. 1996, ApJ, 470, 131

Szapudi, I., Meiksin, A. & Nichol, R.C. 1996, ApJ, 473, 15

Taylor, A.N. & Watts, P.I.R. 2000, MNRAS, 314, 92

Tormen, G. & Bertschinger, E. 1996, ApJ, 472, 14

Xu, W., Fang, L.Z. & Wu, X.P. 2000, ApJ, 532, 728

Yang, X.H., Feng, L.L., Chu, Y.Q. & Fang, L.Z. 2001a, ApJ, 553, 1

Yang, X.H., Feng, L.L., Chu, Y.Q. & Fang, L.Z. 2001b, ApJ, 560, 549

Yang, X.H., Feng, L.L., Chu, Y.Q. & Fang, L.Z. 2002, ApJ, 566, 630

Zhan, H. & Fang, L.Z. 2002, ApJ, 566, 9

Zhan, H., Jamkhedkar, P. & Fang, L.Z. 2001, ApJ, 555, 58

This preprint was prepared with the AAS LaTeX macros v5.0.

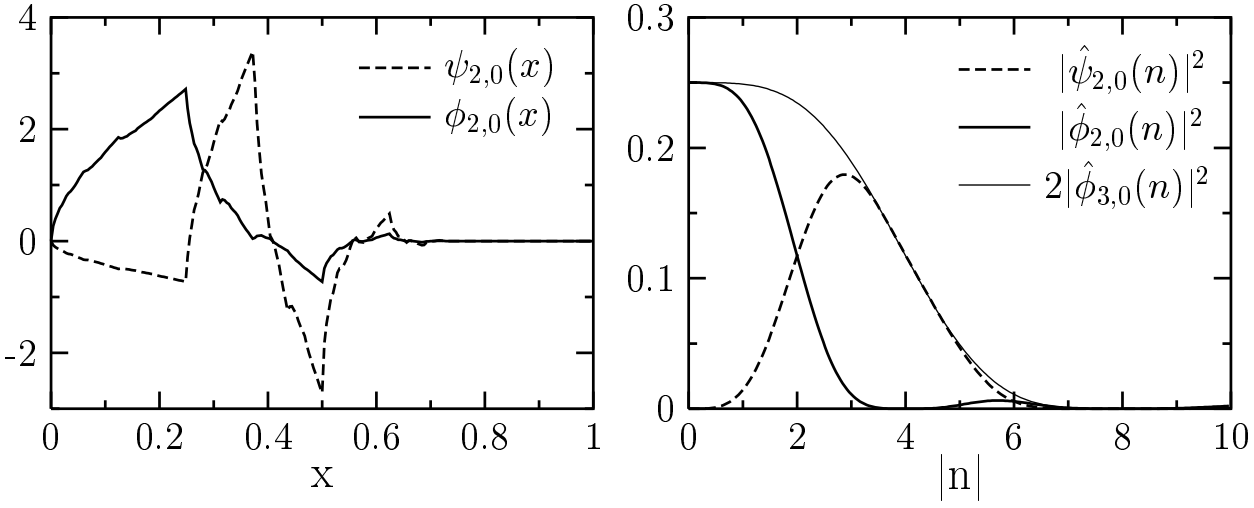

Fig. 1.— The scaling function $\phi_{2,0}(x)$, the wavelet $\psi_{2,0}(x)$, and their Fourier transforms $|\hat{\phi}_{2,0}(n)|^2$, $|\hat{\phi}_{3,0}(n)|^2$, and $|\hat{\psi}_{2,0}(n)|^2$, where $n = kL/2\pi$, and $L = 1$.

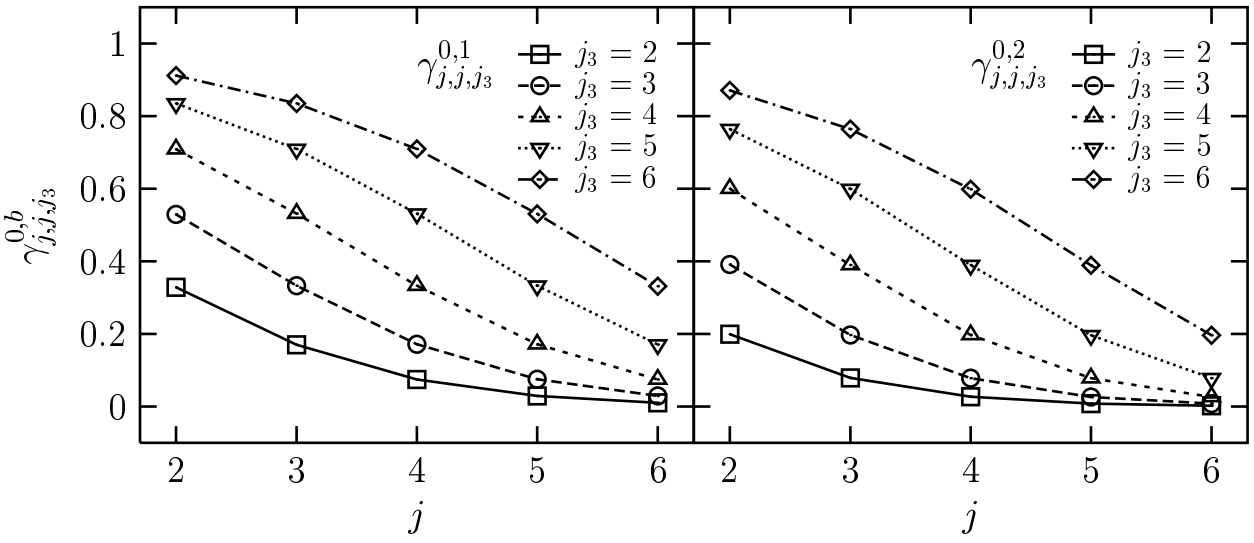

Fig. 2.— The factors of linear redshift distortion $\gamma^{0,1}_{\mathbf{j}}$ and $\gamma^{0,2}_{\mathbf{j}}$ in equation (73). The subscript j_3 indicates the $\hat{x}_3$-direction, or the redshift direction. This convention is followed in all the figures. These factors depend only on the geometry of the DWT cells.

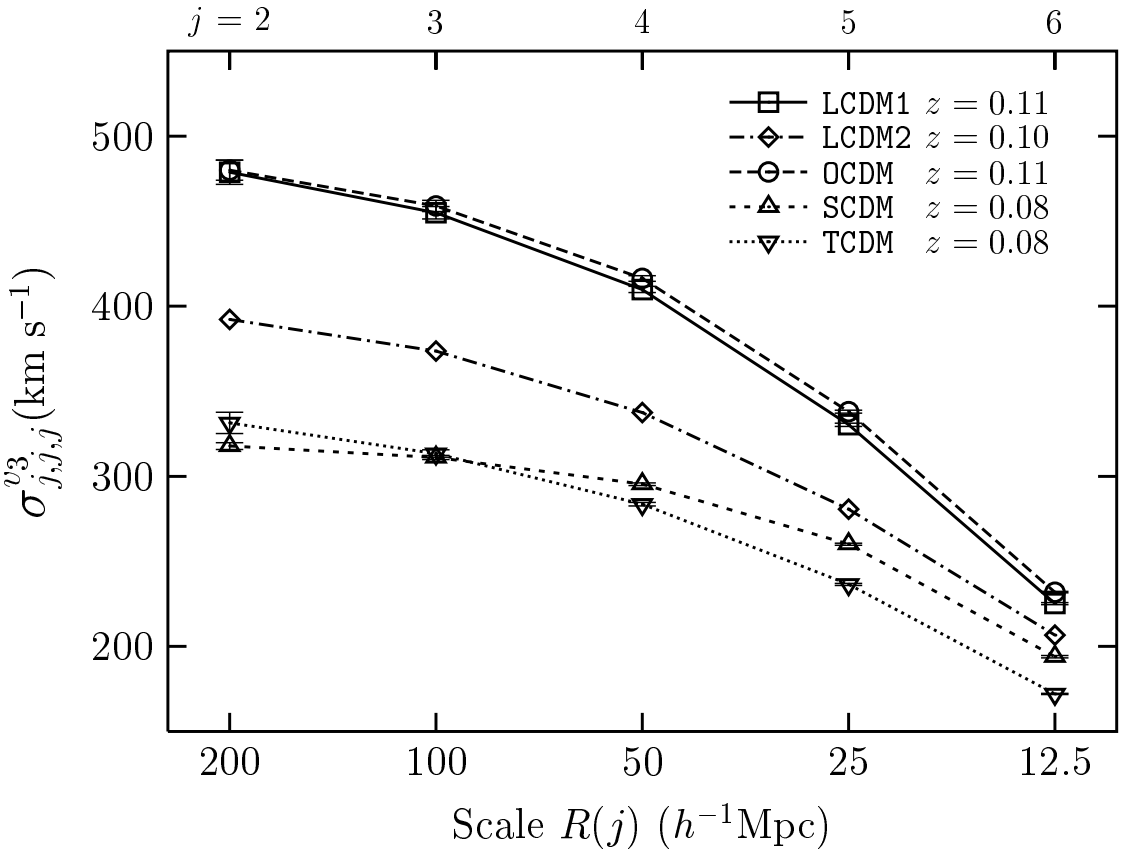

Fig. 3.— The real-space velocity dispersion as defined in equation (42). Only the **j**-diagonal modes, i.e. the modes in cubic cells, are plotted. The units of velocity is physical. The scale in 1-D is $R(j) = 2^{-j}L$, where $L = 800\mathrm{h}^{-1}$Mpc for all models. This definition is assumed in all the figures. The result of LCDM2 model is always plotted without error bars here and below, since there is only one realization for this model.

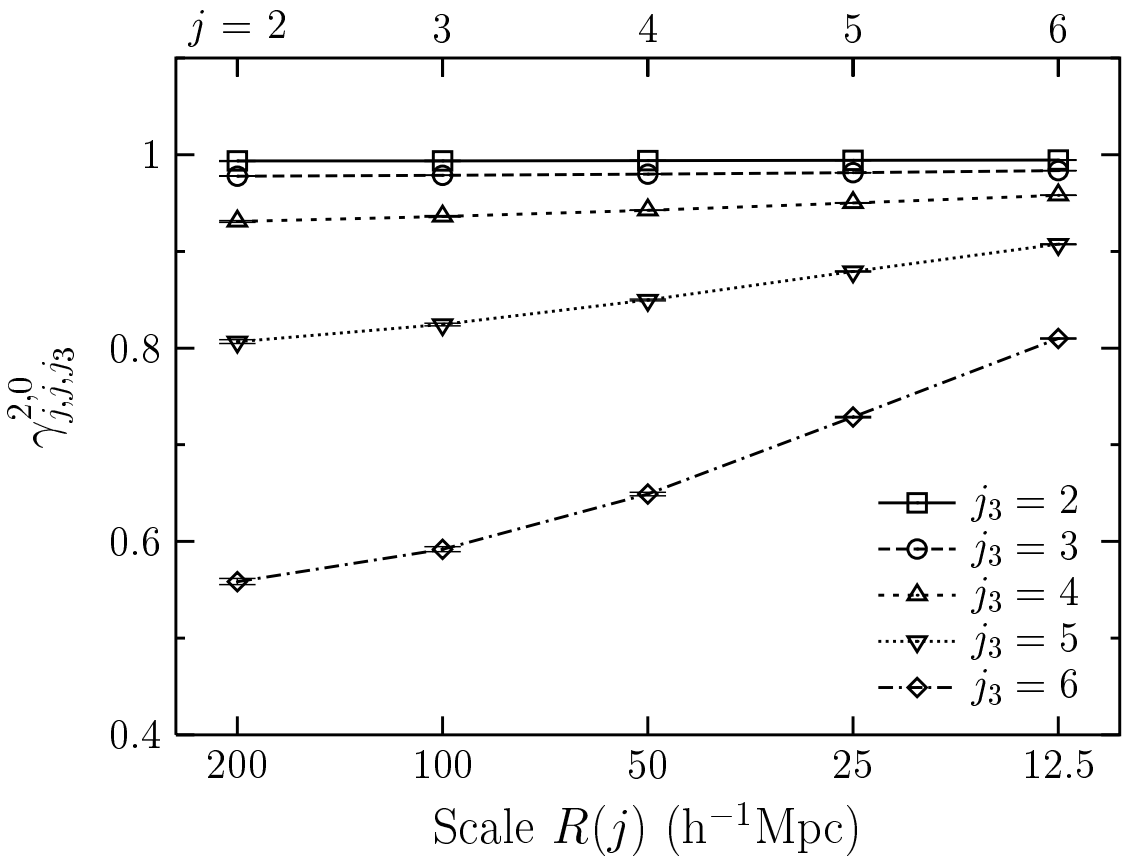

Fig. 4.— The factor of the non-linear redshift distortion $\gamma^{2,0}_{\mathbf{j}}$ in equation (74). It is almost independent of $j_\perp$ when the LOS scale is above 50 h^{-1}Mpc.

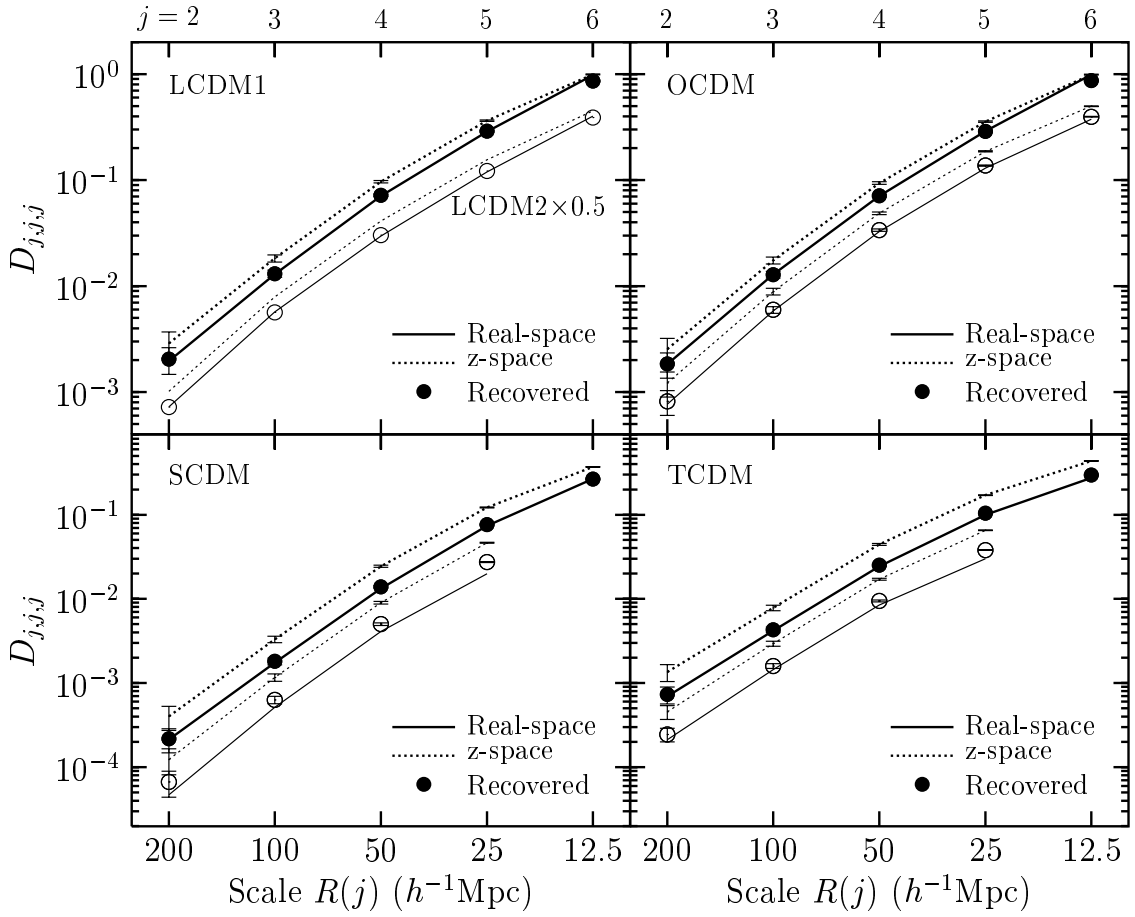

Fig. 5.— The **j**-diagonal DWT 2nd moment $D_{\mathbf{j}}$ recovered using equation (75). The thick lines are at $z = 0.11$, for the LCDM1 and the OCDM models, and 0.08 for the SCDM and the TCDM models. The thin (lower) line in the upper left panel is the LCDM2 model at $z = 0.10$ and multiplied by 0.5. The other thin lines are at $z = 1.13$ for the OCDM model, and 0.71 for the SCDM and the TCDM models. The redshift quoted here is the redshift at the center of each light-cone output. For clarity, the real-space $D_{j,j,j}$ is plotted without symbols or error bars, and the redshift distorted $D_{j,j,j}$ is plotted without symbols. These treatments also apply to Figures 7 and 8. The SCDM and TCDM models have significantly weaker initial power at small wavelengths, so the Poisson noise in the simulations is dominant on small scales at high redshifts. For this reason, the 2nd moment $D_{6,6,6}$ is not shown for the SCDM and the TCDM models at $z = 0.71$.

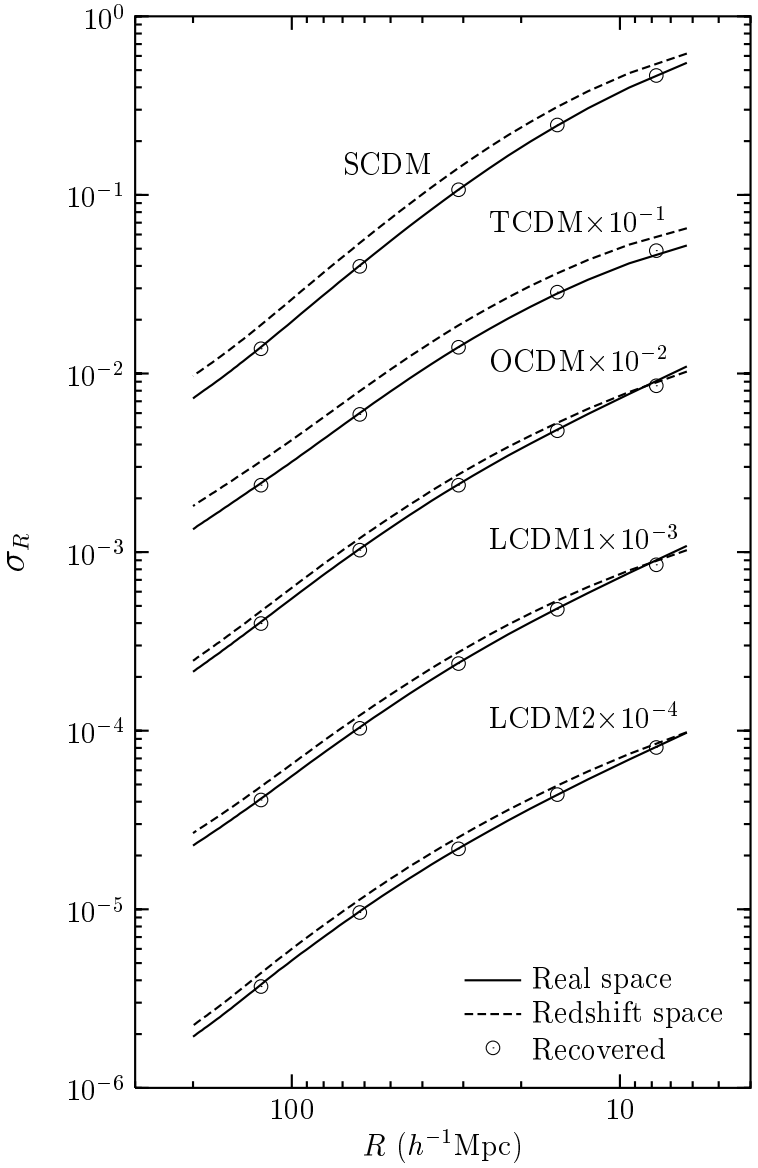

Fig. 6.— The recovery of σ_R, the rms density fluctuation in a sphere of radius R, via $\sigma_R^S \simeq [\gamma^{2,0}_{j,j,j}(1 + 2/3\beta + 1/5\beta^2)]^{1/2}\sigma_R$. The models are shifted for easy reading. The recovery is performed where the volume of the DWT cell conveniently matches that of a sphere of radius R.

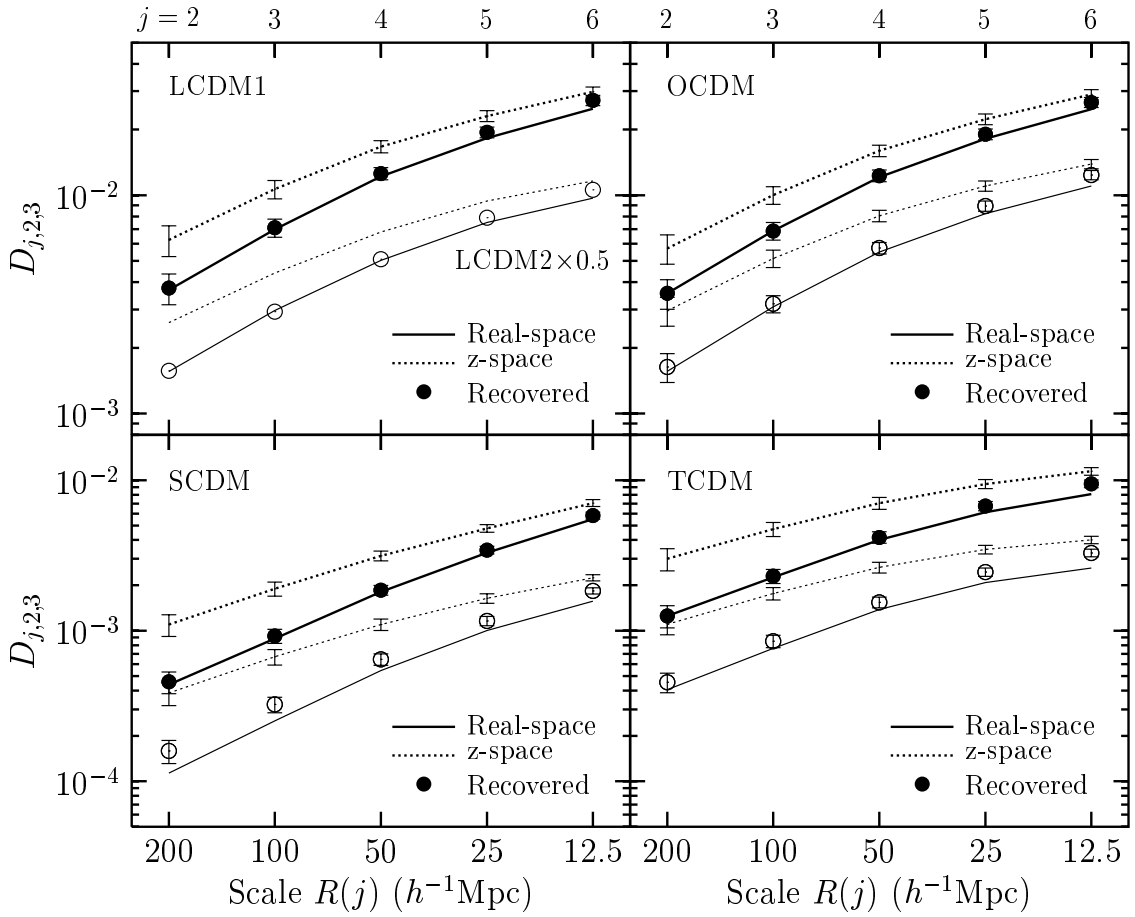

Fig. 7.— Same as Figure 5, except that this is for off-diagonal modes $D_{j,2,3}$.

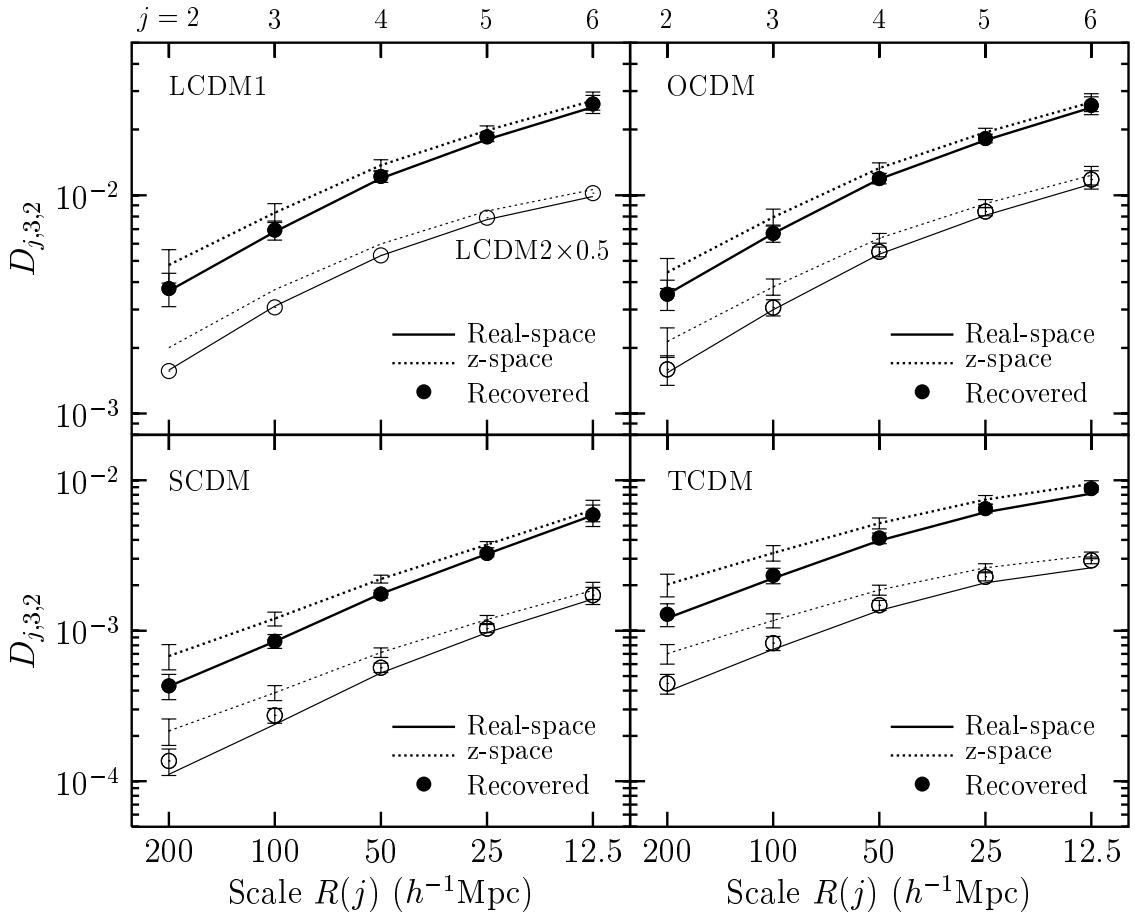

Fig. 8.— Same as Figure 5. except that this is for off-diagonal modes $D_{j,3,2}$.

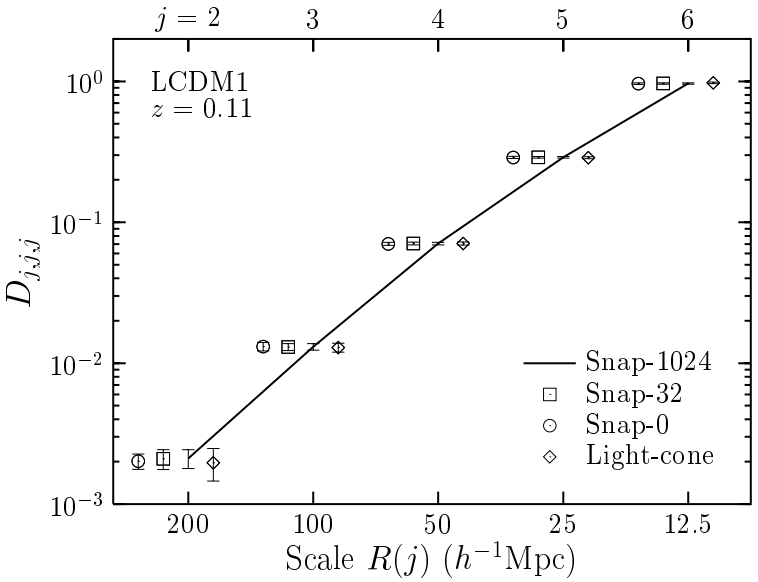

Fig. 9.— Snap-n, $n = 0, 32, 1024$, is calculated from the snapshot output with n random shifts in grid. Snap-0, Snap-32, and the light-cone data are displaced horizontally with respect to Snap-1024 data for easy identification.

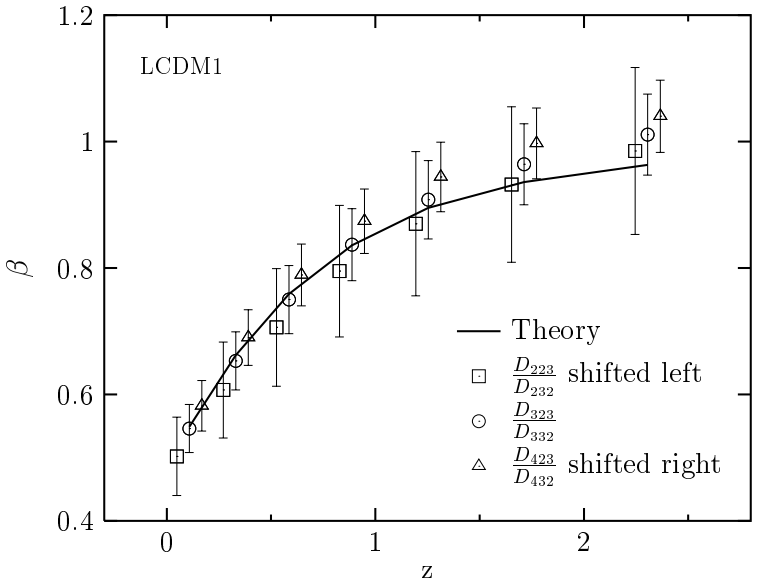

Fig. 10.— The β parameter estimated by estimator eq.(81) for the LCDM1 model.

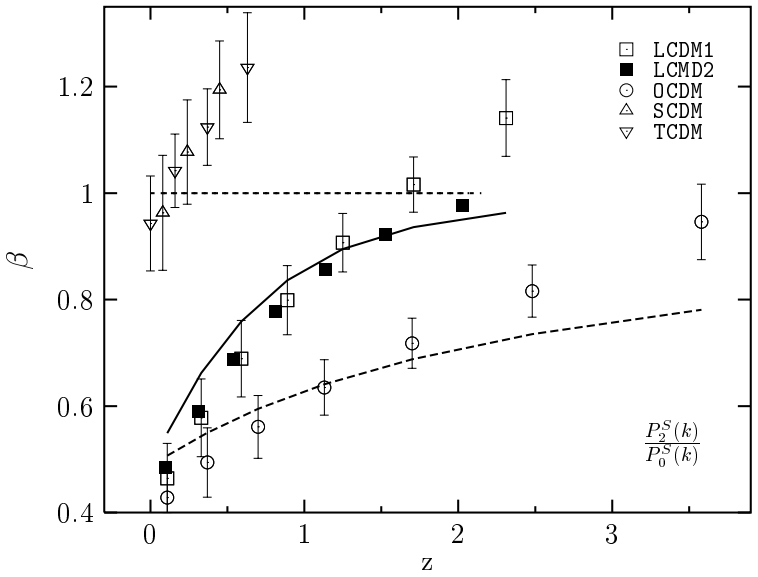

Fig. 11.— The β parameter estimated by quadrupole-to-monopole ratio. The TCDM model is shifted to the left for clear identification. The lines are theoretical β from equation (69) for each model.

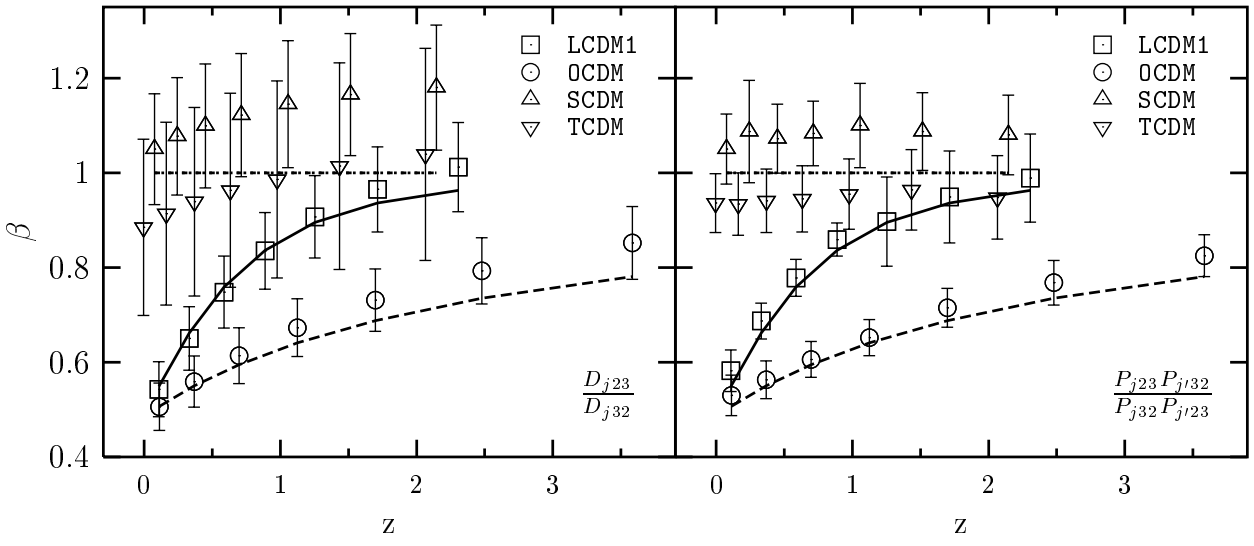

Fig. 12.— The left panel is the β parameter given by an average over that estimated by eq.(81) with modes $j = 2, 3, 4$ for the four models, and the right panel is the β parameter estimated by eq.(84). The TCDM model is shifted to the left for clear identification. The lines are theoretical β from equation (69) for each model.